Under consideration for publication in J. Fluid Mech.

Wall-modelled large-eddy simulation of turbulent channel flow with unstable stratification

Li-Sheng Jiang[1], Ao Xu[1,2] and Heng-Dong Xi[1,2]

[1]Institute of Extreme Mechanics, School of Aeronautics, Northwestern Polytechnical University, Xi'an 710072, PR China

[2]National Key Laboratory of Aircraft Configuration Design, Key Laboratory for Extreme Mechanics of Aircraft of Ministry of Industry and Information Technology, Xi'an 710072, PR China

Corresponding author: Ao Xu, axu@nwpu.edu.cn

(Received xx; revised xx; accepted xx)

Unstable thermal stratification modifies near-wall momentum and heat transport, causing the mean velocity profile to depart from the classical logarithmic law and complicating wall modelling for turbulent mixed convection. We develop a buoyancy-modified logarithmic-quadratic wall model for incompressible Poiseuille–Rayleigh–Bénard (PRB) flow. The model combines an approximately linear relation between the near-wall mean temperature and mean streamwise velocity with a thermally modified mean-gradient representation inspired by mixing-length scaling. *A priori* assessments using wall quantities from the direct numerical simulation (DNS) database of Pirozzoli *et al.* (2017) show that the calibrated wall law reconstructs near-wall velocity and wall-function-equivalent eddy-viscosity profiles. We implement the wall model in wall-modelled large-eddy simulations (WMLES) at friction Reynolds numbers up to $Re_\tau \approx 6000$ and Rayleigh numbers up to $Ra = 10^{10}$. For cases with DNS reference profiles at $Ra = 10^8$ and 10^9, the maximum pointwise absolute relative errors are 3.6% for the mean velocity and 1.9% for the mean temperature. For cases with available DNS global-transport data, the maximum relative deviations in the Nusselt number Nu and skin-friction coefficient C_f are 11.7% and 15.9%, respectively. The WMLES reduces the mesh count by factors of approximately 195–542 relative to the corresponding DNS meshes. For the $Ra = 10^{10}$ and $Ri_b = 0.1$ case, extrapolation of reference DNS resolution strategies gives a mesh count of order 10^{11}, approximately three orders of magnitude larger than the present WMLES mesh count. We also examine how the balance between shear and buoyancy reorganises flow structure, and we identify signatures consistent with the coexistence of streamwise-elongated motions resembling very-large-scale motions (VLSMs) and buoyancy-associated streamwise rolls.

Key words: Turbulent convection, Plumes/thermals, Turbulence simulation

Abstract must not spill onto p.2

1. Introduction

Mixed convection, driven by the interplay between shear and buoyancy, is ubiquitous in both natural and engineering flows. In nuclear-reactor cooling channels, pressure-driven coolant flow may interact with buoyancy induced by wall heating, modifying turbulence and heat transfer (Cotton *et al.* 2001). In the atmospheric boundary layer, mean wind shear interacts with buoyancy generated by surface heating, producing flow structures that range from shear-dominated streaks to streamwise convective rolls (Salesky & Anderson 2018; Jayaraman & Brasseur 2021). In such flows, buoyancy modifies the velocity field, while the resulting fluid motions redistribute heat. This coupling can alter both heat transfer and the spatial organisation of turbulence as the relative strengths of shear and buoyancy vary.

A canonical configuration for studying mixed convection is the Poiseuille–Rayleigh–Bénard (PRB) system (Pirozzoli *et al.* 2017; Madhusudanan *et al.* 2022; Xu *et al.* 2025), which combines pressure-driven Poiseuille flow with buoyancy-driven Rayleigh–Bénard (RB) convection. At fixed Prandtl number Pr, the PRB system is governed by the bulk Reynolds number Re_b and the Rayleigh number Ra, while the resulting wall stress is characterised by the friction Reynolds number Re_τ. The DNS database of Pirozzoli *et al.* (2017) extends to $Re_\tau = 946.41$ and $Ra = 10^9$, and, to the best of our knowledge, these remain the highest Reynolds and Rayleigh numbers attained in DNS of the canonical PRB configuration. Access to still higher Reynolds and Rayleigh numbers would provide greater scale separation and enable the investigation of multiscale interactions relevant to geophysical and industrial flows, but DNS under such conditions remains computationally prohibitive.

Large-eddy simulation (LES) balances accuracy and computational cost by resolving the large energy-containing eddies while modelling the smaller subgrid-scale (SGS) motions. However, wall-resolved LES must still resolve the steep gradients in the near-wall region. Estimates for high-Reynolds-number wall-resolved LES indicate that the inner layer can account for most of the grid points (Piomelli & Balaras 2002). Wall-modelled LES (WMLES) alleviates this bottleneck by coupling a near-wall model with an outer-region LES, thereby reducing grid requirements by orders of magnitude (Bose & Park 2018). The accuracy of WMLES depends not only on the wall-stress closure itself but also on its coupling to the outer LES, including the choice of matching height and grid resolution (Kawai & Larsson 2012; Hu *et al.* 2024). Recent developments have further highlighted the importance of maintaining the near-wall total-shear-stress balance in mitigating log-layer mismatch (Liu *et al.* 2025), as well as the potential of physics-informed, data-assisted corrections for non-equilibrium near-wall effects (Zhang *et al.* 2025). WMLES of high-Reynolds-number neutral atmospheric boundary layers over homogeneous and heterogeneous rough surfaces have also shown that coupled wall-stress and subgrid-scale treatments can capture the wall shear stress, logarithmic mean-velocity profiles and turbulence spectra across different surface conditions (Liu *et al.* 2026).

Earlier temperature wall-function studies addressed mixed convection by blending forced- and natural-convection profiles in vertical channels (Balaji *et al.* 2008) and by evaluating a modified forced-convection wall function in steady Reynolds-averaged simulations around a heated cube (Defraeye *et al.* 2012). Thermal wall treatments based on the sublayer-resistance formulation of Jayatilleke (1969) have also been used in LES of thermally stratified urban flows (Aliabadi *et al.* 2017; Boppana *et al.* 2014). More generally, WMLES formulations for turbulent heat transfer have incorporated models for both wall shear stress and wall heat flux on strongly under-resolved near-wall meshes (Kuwata & Suga 2021). For convective atmospheric boundary layers, Salesky & Anderson (2018) employed a wall-stress model based on Monin–Obukhov similarity theory (MOST), which introduces stability corrections to the logarithmic wall law. Wang *et al.* (2024) assessed LES wall modelling for Rayleigh–Bénard convection using both *a priori* and *a posteriori* tests of surface shear stress and heat flux, and demonstrated limitations of conventional Monin–Obukhov-based treatments under natural-convection conditions. These approaches provide useful treatments of buoyancy effects on near-wall momentum and heat transfer, but they were not developed specifically for the finite-height, two-wall PRB configuration. Scagliarini *et al.* (2015) derived a buoyancy-modified law of the wall for unstably stratified turbulent channel flow. Their formulation provides an important reference for PRB flow, but it is derived for the logarithmic region using asymptotic and local-equilibrium assumptions. As discussed below, these assumptions can become restrictive under strongly buoyancy-dominated conditions and at finite friction Reynolds numbers, where the mean velocity profile departs substantially from classical logarithmic scaling. We therefore seek a wall model for incompressible PRB flow that couples momentum and heat transfer and represents buoyancy-induced changes in the mean velocity profile. Accurate predictions of the wall stress and heat flux are particularly important because errors in the near-wall transport can alter the kinetic-energy distribution and the organisation of large-scale motions in the outer layer.

In this work, we develop a buoyancy-modified logarithmic-quadratic wall model for the canonical PRB configuration. Its functional form and empirical parameters are assessed using the available PRB DNS database before application in WMLES up to $Re_\tau \approx 6000$ and $Ra = 10^{10}$. These simulations examine the spatial organisation and scale-dependent signatures of very-large-scale motions (VLSMs) and buoyancy-driven thermal structures. The remainder of this paper is organised as follows. In §2, we introduce the mixing-length-inspired mean-gradient model and assess its functional form *a priori* against the available DNS data and two reference models. In §3, we describe the computational setup, numerical methods, and the *a posteriori* validation of the WMLES framework. In §4, we analyse the flow structures and their spectral signatures across the investigated regimes. In §5, we summarise the main findings of the present work.

2. Formulation and *a priori* assessment of the buoyancy-modified wall model

2.1. *Formulation of the logarithmic-quadratic wall model*

In purely shear-driven channel flow, the near-wall velocity follows a linear law in the viscous sublayer and a logarithmic law in the logarithmic region. Under unstable stratification, with a hot lower wall and a cold upper wall, temperature gradients generate density differences that drive upward and downward motions. These motions couple the velocity and temperature fields, causing the mean velocity to deviate from the classical wall law. To quantify this deviation and assess the applicability of the classical scaling, we examine DNS data for the PRB system from Pirozzoli *et al.* (2017) using the logarithmic-law diagnostic function $y^+\mathrm{d}U^+/\mathrm{d}y^+$. The DNS data considered here correspond to $Pr = \nu/\alpha = 1$, where ν and α are the kinematic viscosity and thermal diffusivity. The strength of buoyancy relative to shear is measured by the bulk Richardson number $Ri_b = Ra/(Re_b^2 Pr)$, where Ra is the Rayleigh number and $Re_b = 2hu_b/\nu$ is the Reynolds number based on the full channel height $2h$ and bulk velocity u_b. For a classical logarithmic velocity profile, this diagnostic function is constant at $1/\kappa$, giving a plateau at 2.5 for $\kappa = 0.4$. Since finite-Reynolds-number effects can also influence the development of this plateau (Pirozzoli *et al.* 2016; Monkewitz & Nagib 2023), we consider how the diagnostic profiles vary with Ri_b when assessing departures from the classical scaling. These Ri_b-dependent variations, shown in figure 1, therefore motivate a buoyancy-dependent correction to the classical wall law over the near-wall range considered here. Note that mean temperature–velocity

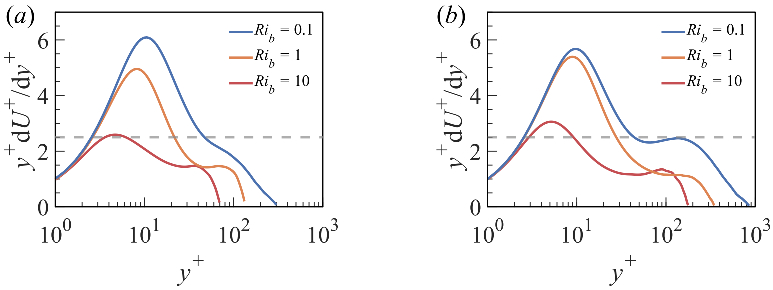

Figure 1. Logarithmic-law diagnostic function for the PRB system computed from the DNS data of Pirozzoli *et al.* (2017) for (*a*) $Ra = 10^7$ and (*b*) $Ra = 10^8$. The horizontal dashed line marks the classical logarithmic-law value $1/\kappa = 2.5$, corresponding to $\kappa = 0.4$.

relations have recently been developed for thermal wall modelling in compressible laminar and turbulent wall flows (Chen *et al.* 2025). For passive-scalar transport in incompressible wall-bounded turbulence, Sun & Fu (2026) developed a mean-temperature model based on the relationship between momentum and thermal eddy diffusivities over a wide range of Prandtl numbers. These formulations concern thermal-transport settings distinct from the present unstably stratified PRB flow, in which temperature is an active scalar that modifies the momentum field through buoyancy.

To express the thermal correction in terms of the mean velocity, we seek a near-wall relation between the mean temperature and mean streamwise velocity. We first consider the heated lower wall at $y = 0$. With $T^* = (T - T_c)/\varDelta T$ and $\varDelta T = T_h - T_c$, we have $T^* = 1$ at the wall. We define the dimensionless local temperature–velocity slope as

$$\frac{\mathrm{d}T^*}{\mathrm{d}U^+} = \frac{\mathrm{d}T^*/\mathrm{d}y^+}{\mathrm{d}U^+/\mathrm{d}y^+}, \tag{2.1}$$

where $U^+ = U/u_\tau$, $y^+ = yu_\tau/\nu$ and $u_\tau = (\tau_w/\rho)^{1/2}$, with ρ the fluid density and ν the kinematic viscosity. Here, $U(y)$ and $T(y)$ denote the DNS mean profiles of Pirozzoli *et al.* (2017), obtained by averaging over the homogeneous streamwise–spanwise planes and over time. The derivatives in equation (2.1) are evaluated from these mean profiles. As shown in figure 2, the local slope varies weakly over a finite near-wall range in the cases examined. This observation motivates an approximately linear relation between the mean temperature and mean streamwise velocity over this range,

$$T \simeq a + bU. \tag{2.2}$$

The coefficients a and b are determined by matching the wall value and the ratio of the wall gradients. The no-slip and thermal boundary conditions, $U(0) = 0$ and $T(0) = T_h$, give $a = T_h$. Matching the slope at the wall gives

$$b = \left.\frac{\mathrm{d}T/\mathrm{d}y}{\mathrm{d}U/\mathrm{d}y}\right|_{y=0} = -\frac{\mu q_w}{k\tau_w}, \tag{2.3}$$

where q_w and τ_w denote the mean wall heat-flux and shear-stress magnitudes, respectively; at the heated lower wall,

$$q_w = -k\left.\frac{\mathrm{d}T}{\mathrm{d}y}\right|_{y=0} > 0, \qquad \tau_w = \mu\left.\frac{\mathrm{d}U}{\mathrm{d}y}\right|_{y=0} > 0.$$

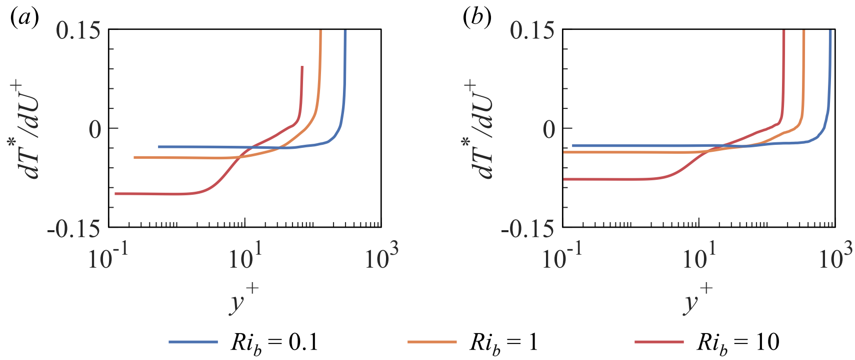

Figure 2. Wall-normal variation of the local dimensionless temperature–velocity slope defined in equation (2.1), at (*a*) $Ra = 10^7$ and (*b*) $Ra = 10^8$. The derivatives are computed from the plane- and time-averaged DNS temperature and velocity profiles of Pirozzoli *et al.* (2017).

Here, μ is the dynamic viscosity and k is the thermal conductivity. Equation (2.2) therefore becomes

$$T \simeq T_h - \frac{\mu q_w}{k\tau_w} U. \tag{2.4}$$

In dimensionless form,

$$T^* \simeq 1 + \beta U^+, \qquad \beta = -\frac{Nu_w}{2Re_\tau}, \tag{2.5}$$

where

$$Nu_w = -\left.\frac{\mathrm{d}T^*}{\mathrm{d}y^*}\right|_{y^*=0}, \qquad Re_\tau = \frac{u_\tau h}{\nu},$$

with $y^* = y/H = y/(2h)$, where $H = 2h$ is the full channel height. The quantity Nu_w is computed from the mean wall temperature gradient.

The approximate relation in equation (2.5) provides the temperature–velocity closure used below to construct the buoyancy-modified momentum wall law. The upper-wall relation follows from the reflection transformations $d = 2h - y$ and $T_u^* = (T_h - T)/\varDelta T = 1 - T^*$. Using d as the distance measured from the upper wall into the fluid, together with the magnitudes of the wall heat flux and wall shear stress, gives $T_u^* \simeq 1 + \beta U^+$, with $\beta = -Nu_w/(2Re_\tau)$ and $y^+ = u_\tau d/\nu$ evaluated using the upper-wall quantities. Applying these substitutions to the mean-gradient model below yields the same final velocity wall law at both walls. Figure 3(*a*,*b*) compares this near-wall linear temperature–velocity approximation with the DNS mean profiles, using the corresponding DNS wall quantities to determine β. To quantify the departure from equation (2.5), figure 3(*c*,*d*) shows the residual $r_T(y) = T^*(y) - [1 + \beta U^+(y)]$ as a function of y/h. The departures become more pronounced farther from the wall, particularly for $Ri_b = 10$.

We next introduce a thermally modified mean-gradient model based on mixing-length scaling. The temperature–velocity approximation will be used to close this model in terms of the mean velocity. Continuing with the lower-wall representation, the characteristic velocity and length scales in the neutrally stratified constant-stress layer are $u_m = u_\tau$ and $\ell_m = \kappa y$, respectively. The corresponding mean velocity gradient is

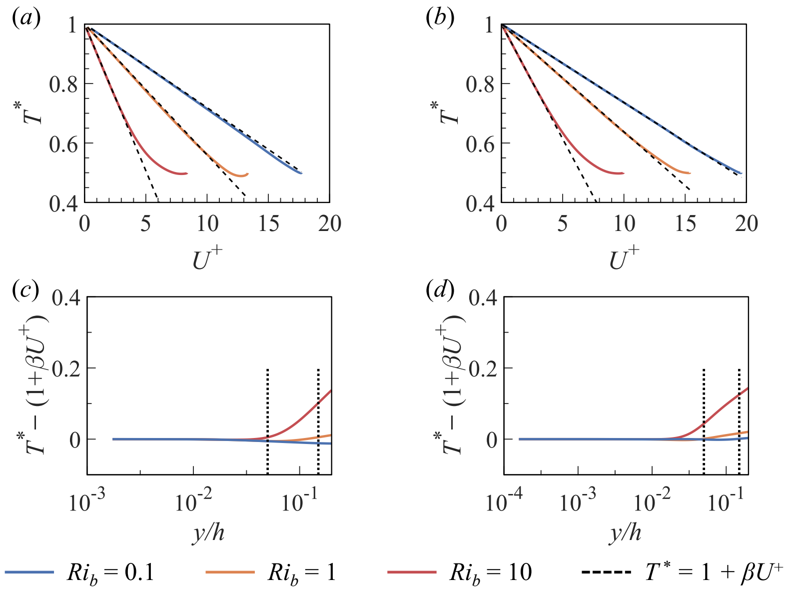

Figure 3. Assessment of the near-wall linear approximation between the mean temperature and mean streamwise velocity against the DNS data of Pirozzoli *et al.* (2017). (*a*,*b*) Comparison of the DNS T^*–U^+ profiles (solid coloured lines) with the approximation $1 + \beta U^+$ in equation (2.5) (black dashed lines), (*c*,*d*) the corresponding signed residuals $T^* - (1 + \beta U^+)$ versus y/h, at (*a*,*c*) $Ra = 10^7$ and (*b*,*d*) $Ra = 10^8$. The vertical lines in (*c*,*d*) mark the wall-model sampling heights y_p/h in the *a priori* comparisons.

$$\frac{\mathrm{d}U}{\mathrm{d}y} = \frac{u_m}{\ell_m} = \frac{u_\tau}{\kappa y}, \tag{2.6}$$

or, in wall units, $\mathrm{d}U^+/\mathrm{d}y^+ = 1/(\kappa y^+)$, which is the classical logarithmic velocity gradient. Under unstable thermal stratification, temperature is an active scalar that modifies turbulent mixing. Motivated by the mixing-length scaling $\mathrm{d}U/\mathrm{d}y \sim u_m/\ell_m$, we retain the wall-distance-based length scale $\ell_m = \kappa y$ and introduce a phenomenological thermal modulation of the characteristic velocity scale,

$$u_m = u_\tau \Phi_T(T^*), \qquad \Phi_T(1) = 1. \tag{2.7}$$

This multiplicative form retains u_τ as the reference velocity determined by the wall stress, while the dimensionless function Φ_T modulates the characteristic velocity scale according to the local thermal state. The condition $\Phi_T(1) = 1$ normalises the thermal modulation to unity at the hot-wall reference state.

The functional form of Φ_T is motivated by the classical free-fall velocity scaling used in thermally driven convection. Under the Boussinesq approximation, the inertial–buoyancy balance $u_f^2/H \sim \beta_T g \varDelta T$ gives the global free-fall velocity scale $u_f = (\beta_T g \varDelta T H)^{1/2}$, where β_T is the thermal expansion coefficient. As a modelling assumption, we introduce a temperature-conditioned velocity scale of the form

$$u_{f,T}(y) = \sqrt{\beta_T g\,[T(y) - T_c]\,H}. \tag{2.8}$$

Normalising by u_f gives

$$\frac{u_{f,T}(y)}{u_f} = \left[\frac{T(y) - T_c}{\mathit{\Delta} T}\right]^{1/2} = (T^*)^{1/2}. \tag{2.9}$$

We adopt the phenomenological thermal modulation $\varPhi_T(T^*) = (T^*)^{1/2}$, so that $u_m = u_\tau (T^*)^{1/2}$. Substituting this thermal modulation into the gradient representation $\mathrm{d}U/\mathrm{d}y = u_m/\ell_m$ with $\ell_m = \kappa y$ gives

$$\frac{\mathrm{d}U^+}{\mathrm{d}y^+} = \frac{1}{\kappa y^+} (T^*)^{1/2}. \tag{2.10}$$

Using the near-wall linear approximation (2.5), $T^* \simeq 1 + \beta U^+$, to close equation (2.10) gives the model equation

$$\frac{\mathrm{d}U^+}{\mathrm{d}y^+} = \frac{1}{\kappa y^+} \left(1 + \beta U^+\right)^{1/2}. \tag{2.11}$$

For finite U^+, the limit $\beta \to 0$ gives $T^* \to 1$ and $\varPhi_T \to 1$, so equation (2.11) reduces to the classical logarithmic velocity gradient, $\mathrm{d}U^+/\mathrm{d}y^+ = 1/(\kappa y^+)$. For $\beta \neq 0$, integration of equation (2.11) gives

$$U^+ = \frac{\left[\frac{\beta}{2}\left(\frac{1}{\kappa}\ln y^+ + B\right)\right]^2 - 1}{\beta}, \tag{2.12}$$

where $\kappa = 0.4$ is the von Kármán constant and B is the integration constant for a given case. The pointwise effective values $B_{\mathrm{eff}}(y)$, inferred from the DNS profiles by inverting equation (2.12) at each wall-normal position, exhibit substantial wall-normal variation and also depend strongly on Ri_b and Ra, as shown in figure 4(*a*–*c*). This strong dependence complicates the calibration of B. We therefore introduce the rescaled integration parameter $C = \beta B/2$ and rewrite equation (2.12) as

$$U^+ = \frac{\left(\frac{\beta}{2\kappa}\ln y^+ + C\right)^2 - 1}{\beta}. \tag{2.13}$$

By contrast, the corresponding pointwise effective parameter $C_{\mathrm{eff}}(y) = \beta B_{\mathrm{eff}}(y)/2$ remains close to unity and exhibits substantially smaller absolute wall-normal and Ra-dependent variations within the available DNS database (figure 4(*d*–*f*)). Note that the profiles $B_{\mathrm{eff}}(y)$ and $C_{\mathrm{eff}}(y)$ describe the parameter values required to match the DNS at each position, whereas the wall law uses one linked pair of casewise constants B and C. In Appendix A, we quantify the relative variations of the pointwise effective parameters $B_{\mathrm{eff}}(y)$ and $C_{\mathrm{eff}}(y)$ across Rayleigh numbers at fixed wall-normal position. We also examine how variations in β and the wall-normal arithmetic average of B_{eff} partially offset each other in the corresponding average of C_{eff}. This reduced variation motivates the use of C in the final formulation. Because equation (2.13) is quadratic in $\ln y^+$, we refer to it as the logarithmic-quadratic wall law.

We next examine the $\beta \to 0$ asymptotic limit of the logarithmic-quadratic wall law. The reference profile is the classical logarithmic law $U^+ = \kappa^{-1}\ln y^+ + B_{\log}$, where $B_{\log}$ is the additive constant, distinct from the integration constant B in equation (2.12). Expanding equation (2.13) separates the constant, logarithmic and quadratic contributions:

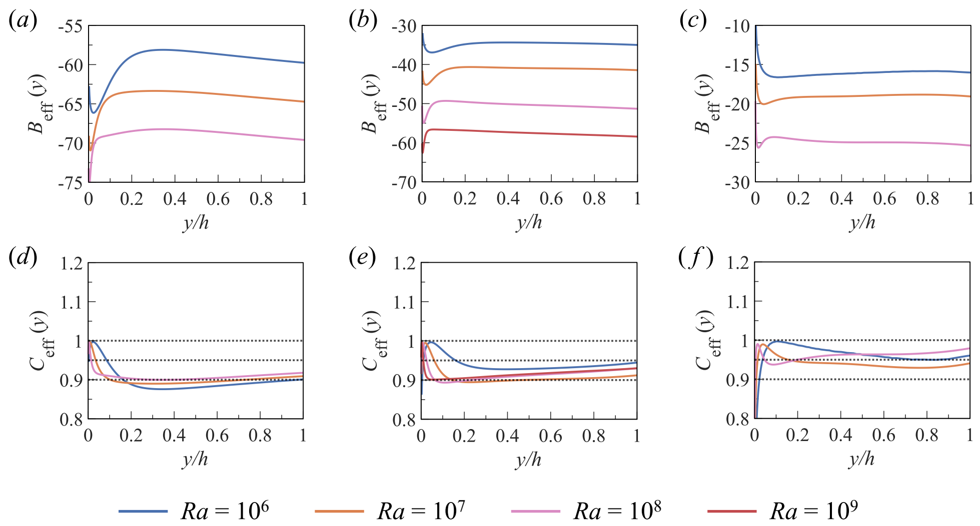

Figure 4. Pointwise effective parameters inferred from the DNS mean velocity profiles of Pirozzoli *et al.* (2017). (*a–c*) $B_{\text{eff}}(y)$ and (*d–f*) $C_{\text{eff}}(y) = \beta B_{\text{eff}}(y)/2$ versus wall-normal distance, with (*a,d*) $Ri_b = 0.1$, (*b,e*) $Ri_b = 1$, and (*c,f*) $Ri_b = 10$. These pointwise effective values are obtained by rearranging equations (2.12) and (2.13) using the DNS mean velocity profile $U^+(y^+)$. The horizontal dotted lines in (*d–f*) indicate $C = 0.90$, 0.95, and 1.00; the first two correspond to the calibrated values used below, while $C = 1.00$ marks the limiting value as $\beta \to 0$.

$$U^+ = \frac{C^2 - 1}{\beta} + \frac{C}{\kappa} \ln y^+ + \frac{\beta}{4\kappa^2} \left(\ln y^+\right)^2 . \tag{2.14}$$

The term quadratic in $\ln y^+$ vanishes as $\beta \to 0$, and recovering the classical logarithmic slope requires $C \to 1$. The intercept $(C^2 - 1)/\beta$ also depends on the rate at which C approaches unity. Matching this intercept to $B_{\log}$ therefore requires

$$C = 1 + \frac{\beta B_{\log}}{2} + o(\beta).$$

Under this condition, equation (2.14) recovers the classical logarithmic law. For $\beta = -Nu_w/(2Re_\tau) < 0$ and $B_{\log} > 0$, this scaling places C slightly below unity for sufficiently small $|\beta|$. The finite-stratification values of C used below are instead calibrated over the investigated PRB cases.

2.2. *A priori assessment against DNS*

We first compare the calibrated logarithmic-quadratic profiles with the DNS mean streamwise velocity profiles, as shown in figure 5. Across each fixed-Ra sequence, increasing Ri_b is accompanied by flatter profiles and a lower centreline velocity in friction units, $U_c^+ = U(h)/u_\tau$. At fixed Ra and $Pr = 1$, increasing Ri_b also reduces Re_b; these comparisons therefore do not isolate the response of the dimensional centreline velocity to buoyancy at fixed bulk Reynolds number. The quadratic dependence on $\ln y^+$ in equation (2.13) allows the slope $\mathrm{d}U^+/\mathrm{d}\ln y^+$ to vary with wall-normal distance, providing a correction to the constant slope of the classical logarithmic law. The comparisons at $Ra = 10^7$ and 10^8 assess whether this functional form can describe the changes in profile

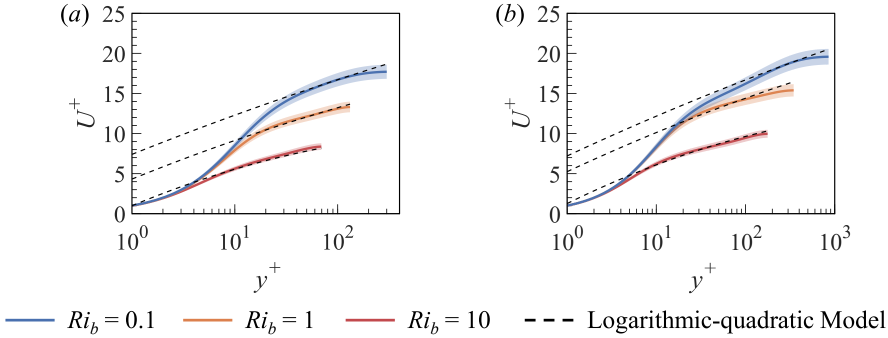

Figure 5. *A priori* assessment of the logarithmic-quadratic law against the DNS data of Pirozzoli *et al.* (2017) for (*a*) $Ra = 10^7$ and (*b*) $Ra = 10^8$. The shaded bands indicate pointwise deviations of ±5% from the DNS profiles. The model uses $\kappa = 0.4$, with $C = 0.90$ for $Ri_b = 0.1$ and 1, and $C = 0.95$ for $Ri_b = 10$.

shape across the different Ri_b regimes. Here, we use $C = 0.90$ for the investigated $Ri_b = 0.1$ and 1 cases, and $C = 0.95$ for $Ri_b = 10$, with both values obtained by offline calibration against the available PRB DNS database.

We compare how three DNS-calibrated functional forms reconstruct the mean velocity profile *a priori*: the proposed model, the model of Scagliarini *et al.* (2015), and the Businger–Dyer MOST implementation specified below. The proposed profile is given by equation (2.13), with $\beta = -Nu_w/(2Re_\tau)$ evaluated from DNS wall quantities and C calibrated against the same DNS database. For comparison, the Scagliarini model expresses the velocity profile as

$$U^+\left(y^+\right) = \frac{1}{\kappa}\ln\left(\frac{y^+}{1+\kappa_C\, y^+}\right) + C_1, \tag{2.15}$$

where $\kappa_C\left(Ra, Re_\tau\right) = A_{\mathrm{Sc}} Ra/(Re_\tau^4 Pr^2)$ is the model's buoyancy coefficient, $\kappa = 0.42$, and $A_{\mathrm{Sc}} = 2.5$ is its fixed empirical constant. The additive constant C_1 is determined separately for each case from the corresponding DNS mean-velocity profile. For the MOST comparison in the lower-wall representation, we implement the following mean-velocity profile with the integrated stability correction Ψ_m:

$$U\left(y\right) = \frac{u_\tau}{\kappa}\left[\ln\left(\frac{y}{y_0}\right) - \Psi_m\left(\frac{y}{L_O}\right)\right], \tag{2.16}$$

where $y_0 > 0$ is an effective intercept parameter, expressed as an equivalent momentum roughness length, and $\zeta = y/L_O$ is the dimensionless stability parameter. In the present smooth-wall PRB flow, y_0 controls the logarithmic intercept. We use the positive Obukhov scale $L_O = u_\tau^3/(\beta_T g Q) > 0$, where Q is the global kinematic vertical temperature flux. The corresponding dimensional heat flux q is defined as positive in the upward ($+y$) direction, with $Q = q/(\rho_0 c_p)$ and $\alpha = k/(\rho_0 c_p)$, where ρ_0 is the reference density, c_p is the specific heat capacity at constant pressure, and k is the thermal conductivity. The global kinematic vertical temperature flux Q used in the Obukhov scale is obtained from the reported global Nusselt number as

$$Q = \frac{\alpha \Delta T}{2h} Nu, \qquad q = \rho_0 c_p Q = \frac{k \Delta T}{2h} Nu. \tag{2.17}$$

For the *a priori* MOST profiles, the corresponding DNS value of this global Nu is used. For the present unstable flows, the signed global heat transport gives $Q > 0$, so that $\zeta > 0$ denotes unstable stratification in this implementation. The stability correction is given by

$$\Psi_m(\zeta) = 2\ln\left(\frac{1+x}{2}\right) + \ln\left(\frac{1+x^2}{2}\right) - 2\arctan(x) + \frac{\pi}{2},$$

with $x = (1+16\zeta)^{1/4}$ and $\kappa = 0.35$. The positive definition of L_O, the value $\kappa = 0.35$ and the Businger–Dyer coefficient 16 follow the convention used by Pirozzoli *et al.* (2017) for PRB flow. The relation adopted here is the integrated Businger–Dyer momentum flux–profile relation. The underlying gradient relation originates from Businger *et al.* (1971) and Dyer (1974), while the integrated form of the stability correction used here follows Paulson (1970). An overview of Monin–Obukhov similarity formulations is provided by Foken (2006). For the *a priori* comparison in figure 6, y_0 is fitted separately for each case using the corresponding DNS mean-velocity profile. Any constant associated with the lower integration limit is absorbed into the fitted effective intercept y_0. The MOST comparisons below refer specifically to the implementation in equation (2.16).

As shown in figure 6, all three formulations agree reasonably well with the DNS data in the shear-dominated regime ($Ri_b = 0.1$). Under stronger buoyancy, particularly at $Ri_b = 10$ and 100, the implemented Businger–Dyer MOST profile and the Scagliarini model overpredict the mean velocity over the near-wall matching ranges indicated in figure 6, whereas the proposed functional form provides a closer reconstruction of the DNS profiles. We also express the same profile comparison in terms of the wall-function-equivalent eddy viscosity,

$$\frac{\nu_{t,\mathrm{WF}}}{\nu} = \frac{y^+}{U^+} - 1, \tag{2.18}$$

obtained by representing the wall shear stress magnitude as $\tau_w = \rho\left(\nu + \nu_{t,\mathrm{WF}}\right) U/y$. Here, U/y is the wall-to-point velocity gradient magnitude for the lower-wall mean profile, distinct from the local gradient $\mathrm{d}U/\mathrm{d}y$. Figure 7 shows that the implemented Businger–Dyer MOST profile and the Scagliarini model underestimate this quantity in the matching region under strong buoyancy, whereas the proposed model gives a closer reconstruction.

The differences in profile reconstruction may reflect the models' assumptions and calibration. First, the model of Scagliarini *et al.* (2015) was derived specifically for the logarithmic region. Its derivation uses the asymptotic $Re_\tau \to \infty$ form of the total-stress balance. It further assumes an approximately constant Reynolds stress, local equilibrium between turbulent-energy production and dissipation, and a Prandtl mixing length proportional to y. The buoyancy-production term is closed using a local gradient-diffusion approximation for the turbulent heat flux together with an assumed logarithmic mean-temperature gradient. These assumptions may be restrictive when the DNS velocity and temperature profiles depart substantially from logarithmic behaviour. In particular, the case $Ri_b = 100$ at $Ra = 10^8$ has $Re_\tau \approx 96$, so a well-developed asymptotic logarithmic region cannot be assumed. Second, the Businger–Dyer relation underlying the MOST implementation used here was developed primarily from atmospheric constant-flux surface-layer observations. It assumes that the dimensionless mean-velocity gradient is a universal function of the single local stability parameter y/L_O. In the present PRB system, finite-height and two-wall confinement may introduce an outer-scale dependence and non-local momentum and heat transport not captured by a relation based on y/L_O alone. Related limitations of Monin–Obukhov-based wall treatments under natural-convection-

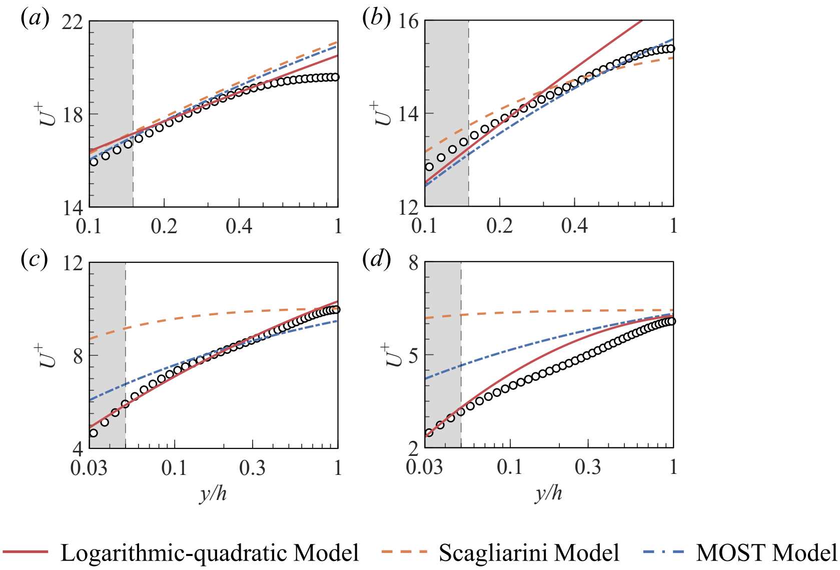

Figure 6. *A priori* comparison of streamwise-velocity profiles U^+ reconstructed using three wall-model functional forms with DNS data of Pirozzoli *et al.* (2017). The MOST curves use the Businger–Dyer implementation in equation (2.16). The DNS-calibrated parameters span $C_1 \in [5.8, 9.0]$ for Scagliarini's model and $C \in [0.9, 1.0]$ for the proposed logarithmic-quadratic model. The fitted MOST intercepts are $y_0^+ = 0.27$, 0.23, 0.22 and 0.07 in (*a*)–(*d*), respectively. (*a*) $Re_b = 10^{4.5}$, corresponding to $Ri_b = 0.1$; (*b*) $Re_b = 10^4$, corresponding to $Ri_b = 1$; (*c*) $Re_b = 10^{3.5}$, corresponding to $Ri_b = 10$; and (*d*) $Re_b = 10^3$, corresponding to $Ri_b = 100$, at $Ra = 10^8$. The shaded regions indicate the near-wall matching ranges considered in the *a priori* comparisons.

dominated conditions have also been identified in *a priori* and *a posteriori* LES wall-model assessments of Rayleigh–Bénard convection (Wang *et al.* 2024). The proposed model uses a mixing-length-based gradient representation over the specified matching interval, incorporating the near-wall linear temperature–velocity approximation and the DNS wall heat flux through β. Together with the calibration of C, these inputs may contribute to the improved profile reconstruction in the matching region.

3. Numerical methodology and *a posteriori* validation

3.1. *Computational setup and governing equations*

We consider incompressible flow between two horizontal walls, with a hot lower wall at temperature T_h located at $y = 0$ and a cold upper wall at temperature T_c located at $y = 2h$. The flow is driven by a spatially uniform streamwise body-force acceleration f_b representing the mean pressure-gradient forcing. A constant bulk flow rate is imposed, and f_b is adjusted dynamically at each time step to maintain the prescribed bulk Reynolds number Re_b. Periodic boundary conditions are imposed in the streamwise and spanwise directions, and no-slip velocity conditions are applied at both walls. The computational domain is $L \times H \times W = 16h \times 2h \times 8h$ in the streamwise (x), wall-normal (y), and spanwise (z) directions, respectively. The flow is characterised by three independent dimensionless numbers: the bulk Reynolds number, $Re_b = 2hu_b/\nu$, where u_b is the bulk velocity; the Rayleigh number, $Ra = (8h^3\beta_T g \mathit{\Delta} T)/(\alpha\nu)$; and the Prandtl number, $Pr = \nu/\alpha$. The strength of buoyancy relative to shear is quantified by the bulk Richardson number $Ri_b =$

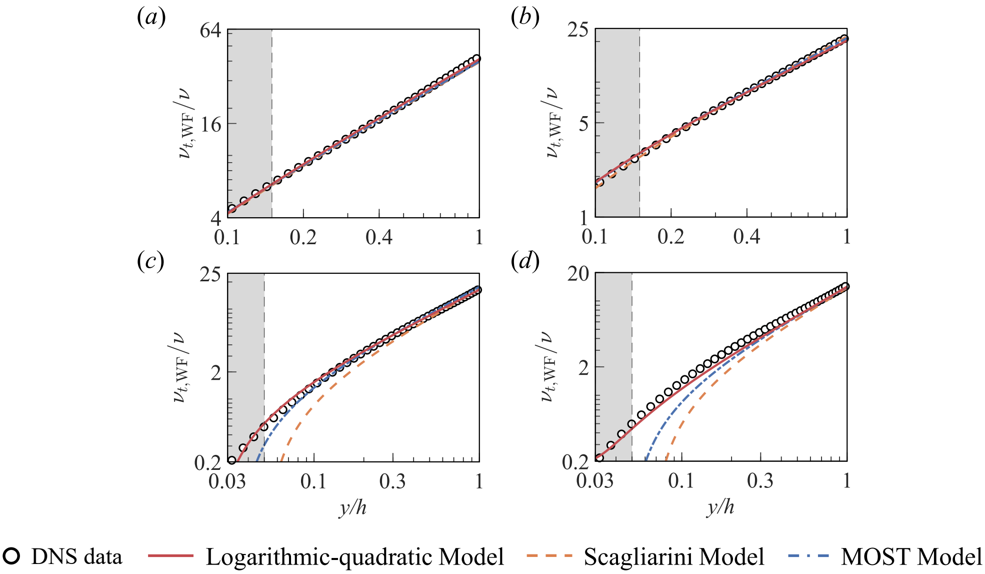

Figure 7. *A priori* comparison of the wall-function-equivalent eddy viscosity $\nu_{t,\mathrm{WF}}/\nu = y^+/U^+ - 1$ from the three wall-model formulations and from the DNS mean profiles of Pirozzoli *et al.* (2017). The MOST curves use the Businger–Dyer implementation in equation (2.16). The velocity profiles use the same DNS-calibrated parameters as in figure 6. (*a*) $Re_b = 10^{4.5}$, corresponding to $Ri_b = 0.1$; (*b*) $Re_b = 10^4$, corresponding to $Ri_b = 1$; (*c*) $Re_b = 10^{3.5}$, corresponding to $Ri_b = 10$; and (*d*) $Re_b = 10^3$, corresponding to $Ri_b = 100$, at $Ra = 10^8$. The shaded regions indicate the near-wall matching ranges considered in the *a priori* comparisons.

$Ra/(Re_b^2 Pr)$. The main parameter study spans $10^8 \le Ra \le 10^{10}$ and $0.1 \le Ri_b \le 10$, with $Pr = 1$ fixed. All simulations are performed using OpenFOAM (version 8) with the transient *buoyantPimpleFoam* solver under the Boussinesq approximation and a subgrid-scale turbulence model. The filtered governing equations are written in component form as

$$\frac{\partial \overline{u_i}}{\partial x_i} = 0, \tag{3.1a}$$

$$\frac{\partial \overline{u_i}}{\partial t} + \frac{\partial \left(\overline{u_i}\,\overline{u_j}\right)}{\partial x_j} = -\frac{1}{\rho_0}\frac{\partial \overline{p}}{\partial x_i} + \nu \frac{\partial^2 \overline{u_i}}{\partial x_j \partial x_j} - \frac{\partial \tau_{ij}^{\mathrm{sgs}}}{\partial x_j} + g\beta_T\left(\overline{T} - T_0\right)\delta_{i2} + f_b\delta_{i1}, \tag{3.1b}$$

$$\frac{\partial \overline{T}}{\partial t} + \frac{\partial \left(\overline{T}\,\overline{u_i}\right)}{\partial x_i} = \alpha \frac{\partial^2 \overline{T}}{\partial x_i \partial x_i} - \frac{\partial J_i^{\mathrm{sgs}}}{\partial x_i}. \tag{3.1c}$$

The SGS kinematic stress and temperature flux are defined by $\tau_{ij}^{\mathrm{sgs}} = \overline{u_i u_j} - \overline{u_i}\,\overline{u_j}$ and $J_i^{\mathrm{sgs}} = \overline{T u_i} - \overline{T}\,\overline{u_i}$. Here, the overbar denotes spatial filtering, repeated indices are summed, and δ_{ij} is the Kronecker delta, with $x_1 = x$, $x_2 = y$ and $x_3 = z$; ρ_0 is the reference density, g is the magnitude of the gravitational acceleration, and $T_0 = T_c$ is the reference temperature in the Boussinesq approximation.

We introduce the nondimensional variables

$$
\begin{aligned}
x_i^* &= \frac{x_i}{2h}, \qquad t^* = \frac{t}{2h/u_b}, \quad u_i^* = \frac{u_i}{u_b}, \\
p^* &= \frac{p}{\rho_0 u_b^2}, \qquad T^* = \frac{T - T_c}{\Delta T}, \quad f_b^* = \frac{f_b}{u_b^2/(2h)}, \\
\tau_{ij}^{\mathrm{sgs}*} &= \frac{\tau_{ij}^{\mathrm{sgs}}}{u_b^2}, \qquad J_i^{\mathrm{sgs}*} = \frac{J_i^{\mathrm{sgs}}}{u_b \Delta T}.
\end{aligned}
\tag{3.2}
$$

Equations (3.1) can then be written in nondimensional form as

$$
\frac{\partial \overline{u_i^*}}{\partial x_i^*} = 0, \tag{3.3a}
$$

$$
\frac{\partial \overline{u_i^*}}{\partial t^*} + \frac{\partial \left(\overline{u_i^*}\,\overline{u_j^*}\right)}{\partial x_j^*} = -\frac{\partial \overline{p^*}}{\partial x_i^*} + \frac{1}{Re_b}\frac{\partial^2 \overline{u_i^*}}{\partial x_j^* \partial x_j^*} - \frac{\partial \tau_{ij}^{\mathrm{sgs}*}}{\partial x_j^*} + \frac{Ra}{Re_b^2 Pr}\overline{T^*}\delta_{i2} + f_b^*\delta_{i1}, \tag{3.3b}
$$

$$
\frac{\partial \overline{T^*}}{\partial t^*} + \frac{\partial \left(\overline{T^*}\,\overline{u_i^*}\right)}{\partial x_i^*} = \frac{1}{Re_b Pr}\frac{\partial^2 \overline{T^*}}{\partial x_i^* \partial x_i^*} - \frac{\partial J_i^{\mathrm{sgs}*}}{\partial x_i^*}. \tag{3.3c}
$$

For the velocity field, we use the wall-adapting local eddy-viscosity (WALE) model (Nicoud & Ducros 1999), while for the temperature field we adopt a constant SGS Prandtl number. The WALE model accounts for strain-rate and rotation-rate contributions through the velocity-gradient tensor. Dynamic and mixed-scale alternatives have been studied for buoyancy-driven turbulence (Lau *et al.* 2013; Yilmaz 2021; Dabbagh *et al.* 2017; Maulik & San 2017). Here we use the fixed algebraic WALE closure for computational robustness; the resolved statistics and global heat-transfer performance are assessed below.

The framework uses separate turbulent Prandtl numbers: Pr_{sgs} for the SGS heat-flux closure and $Pr_{t,\mathrm{wall}}$ for the thermal wall function. These parameters describe different modelled transport contributions and are prescribed independently. The bulk SGS eddy viscosity and thermal diffusivity are denoted by ν_{sgs} and α_{sgs}, respectively, with $\alpha_{\mathrm{sgs}} = \nu_{\mathrm{sgs}}/Pr_{\mathrm{sgs}}$, and we set $Pr_{\mathrm{sgs}} = 0.4$ (Kenjereš & Hanjalić 2006). For the DNS mean profiles, we define the flux–gradient transport coefficients as

$$
\nu_{t,\mathrm{DNS}} = -\frac{\langle u'v' \rangle_{x,z,t}}{\mathrm{d}U/\mathrm{d}y}, \qquad \alpha_{t,\mathrm{DNS}} = -\frac{\langle v'T' \rangle_{x,z,t}}{\mathrm{d}T/\mathrm{d}y},
$$

where $\langle \cdot \rangle_{x,z,t}$ denotes plane and time averaging. We use the DNS-inferred ratio $Pr_{t,\mathrm{DNS}} = \nu_{t,\mathrm{DNS}}/\alpha_{t,\mathrm{DNS}}$, obtained from the data of Pirozzoli *et al.* (2017) and shown in figure 8, to select representative values of the prescribed wall turbulent Prandtl number $Pr_{t,\mathrm{wall}}$. Very close to the wall, both turbulent transport coefficients approach zero and their ratio is ill-conditioned. We instead use the approximately constant portions of the profiles farther from the wall. Across the available DNS range shown in figure 8, the representative plateau values of $Pr_{t,\mathrm{DNS}}$ vary only weakly with Ra at fixed Ri_b. We therefore prescribe $Pr_{t,\mathrm{wall}} = 0.9$ for $Ri_b = 0.1$ and 1 and $Pr_{t,\mathrm{wall}} = 0.7$ for $Ri_b = 10$. These values are retained at higher Ra as a modelling assumption; any additional Ra-dependence outside the available DNS range constitutes an uncertainty of the high-Ra extrapolation. The shaded region in figure 8 indicates the range of wall-adjacent cell-centre locations used as the wall-model sampling heights across the WMLES cases.

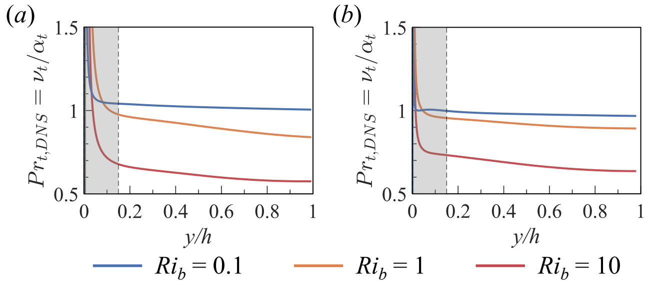

Figure 8. Wall-normal variation of the DNS-inferred turbulent Prandtl ratio $Pr_{t,\mathrm{DNS}} = \nu_{t,\mathrm{DNS}}/\alpha_{t,\mathrm{DNS}}$, obtained from the DNS data of Pirozzoli *et al.* (2017), for (*a*) $Ra = 10^7$ and (*b*) $Ra = 10^8$. The shaded region indicates the range of wall-adjacent cell-centre locations used as the wall-model sampling heights across the WMLES cases.

In all simulations, temporal discretisation uses OpenFOAM's second-order implicit backward scheme. The time step is adjusted to maintain a maximum Courant–Friedrichs–Lewy (CFL) number of 0.8. In each wall-normal column, the control volume adjacent to either wall has a thickness $2y_p$, so that its centroid is located at the prescribed sampling height y_p measured from the wall boundary face. The two wall-adjacent cells are symmetric about the channel centreline. The remaining $N_y - 2$ cells are uniformly spaced in the wall-normal direction, with interior spacing $\Delta y_{\mathrm{int}} = (2h - 4y_p)/(N_y - 2)$. The wall-adjacent cell centres form homogeneous (x–z) planes at the wall-model sampling height y_p. All statistics are collected over $500t_f$ after an initial $500t_f$ transient, where $t_f = H/u_f = \sqrt{H/(g\beta_T \Delta T)}$ is the free-fall time. At each time step, the wall-model inputs are obtained by averaging the resolved cell-centred fields over the homogeneous sampling plane, separately for the lower and upper walls. For the lower wall, the friction velocity is evaluated using the time-averaged inputs $\overline{U}_p = \langle U_p(t)\rangle_t = \langle u_x(x, y_p, z, t)\rangle_{x,z,t}$ and $\overline{\nu}_{t,w} = \langle \nu_{t,w}(t)\rangle_t$ as

$$u_\tau = \left[\left(\nu + \overline{\nu}_{t,w}\right) \frac{\overline{U}_p}{y_p} \right]^{1/2}. \tag{3.4}$$

This value is used for the reported friction-based quantities and normalisations. Table 1 lists the simulation parameters and grid settings, and table 2 gives the corresponding spacings in wall units, Δx^+, $\Delta y^+_{\mathrm{int}}$ and Δz^+. The wall model represents unresolved near-wall transport, the outer mesh is intended to resolve energy-containing motions, and the DNS comparisons below assess the resulting statistics. The matching height and grid resolution can influence both the mean-flow accuracy and the convergence behaviour of WMLES (Kawai & Larsson 2012; Hu *et al.* 2024). We therefore assess the adopted grid and matching-height choices *a posteriori* against the available PRB DNS and compare the corresponding spacings with representative WMLES resolutions reported in the literature. For the most demanding case, $Ra = 10^{10}$ and $Ri_b = 0.1$ ($Re_\tau \approx 6000$), the spacings in the channel interior are $\Delta x^+ \approx 128.0$, $\Delta y^+_{\mathrm{int}} \approx 64.0$ and $\Delta z^+ \approx 64.0$. For reference, Bae *et al.* (2019) used $\Delta_i^+ = 210$ for plane-channel WMLES at $Re_\tau \approx 4200$; Chung & McKeon (2010) used $(\Delta x^+, \Delta y^+, \Delta z^+) \approx (340, 85, 340)$ for long-channel WMLES at $Re_\tau = 2000$; and D'Alessandro *et al.* (2025) used $\Delta x^+ = 156$, $\Delta y^+ = 56$ and $\Delta z^+ = 78$ in a channel-flow validation at $Re_\tau \approx 5200$.

Flow case	Re_b	Ra	Ri_b	h/L_O	Re_τ	Nu	C_f	N_x	N_y	N_z
Ra7Re3.5	3162	10^7	1	2.99	130	10.5	1.35×10^{-2}	128	42	128
Ra7Re3.5*	3162	10^7	1	3.02	135	11.9	1.46×10^{-2}	1024	256	512
Ra8Re3.5	3162	10^8	10	36.3	169	28.3	2.30×10^{-2}	256	66	256
Ra8Re3.5*	3162	10^8	10	30.1	179	27.7	2.57×10^{-2}	2560	512	1280
Ra8Re4	10000	10^8	1	4.05	338	25.0	9.13×10^{-3}	256	66	256
Ra8Re4*	10000	10^8	1	3.68	351	25.4	9.86×10^{-3}	2560	512	1280
Ra8Re4.5	31623	10^8	0.1	0.524	792	41.7	5.02×10^{-3}	256	66	256
Ra8Re4.5*	31623	10^8	0.1	0.441	864	45.6	5.98×10^{-3}	2560	512	1280
Ra9Re4	10000	10^9	10	44.9	449	65.0	1.61×10^{-2}	512	102	512
Ra9Re4.5	31623	10^9	1	4.88	893	55.7	6.39×10^{-3}	512	102	512
Ra9Re4.5*	31623	10^9	1	4.44	946	60.3	7.17×10^{-3}	6144	768	3072
Ra9Re5	100000	10^9	0.1	0.603	2180	99.9	3.80×10^{-3}	512	102	512
Ra10Re4.5	31623	10^{10}	10	50.5	1250	158	1.25×10^{-2}	750	152	750
Ra10Re5	100000	10^{10}	1	5.83	2460	139	4.85×10^{-3}	750	152	750
Ra10Re5.5	316228	10^{10}	0.1	0.718	6000	248	2.88×10^{-3}	750	152	750

Table 1. Numerical details of the simulated flow cases. Here, $Re_b = 2hu_b/\nu$ is the bulk Reynolds number; $Ra = (8h^3\beta_T g\Delta T)/(\alpha\nu)$ is the Rayleigh number; $Ri_b = 2\beta_T g\Delta T h/u_b^2$ is the bulk Richardson number; $L_O = u_\tau^3/(\beta_T g Q) > 0$ is the positive Obukhov scale, where $Q = \alpha\Delta T Nu/(2h) > 0$ is the global kinematic vertical temperature flux obtained from the reported Nu; $Re_\tau = hu_\tau/\nu$ is the friction Reynolds number; Nu is the volume- and time-averaged global Nusselt number; and $C_f = 2u_\tau^2/u_b^2 = 8(Re_\tau/Re_b)^2$ is the skin-friction coefficient. The derived quantities $h/L_O = Ra\,Nu/(16Pr^2Re_\tau^3)$ and C_f are evaluated using the retained precision of Nu and Re_τ, with Re_b given by the case definition. For the WMLES entries, N_x, N_y, and N_z denote the numbers of control volumes (cells) in the streamwise, wall-normal, and spanwise directions, respectively; the DNS mesh counts are retained as reported in the source study. The notation RaXReY denotes configurations with $Ra = 10^{\mathrm{X}}$ and $Re_b = 10^{\mathrm{Y}}$. The superscript * indicates the results of Pirozzoli *et al.* (2017).

Flow case	Re_b	Ra	Ri_b	Δx^+	$\Delta y^+_{\mathrm{int}}$	Δz^+	y_p^+	y_p/h
Ra7Re3.5	3162	10^7	1	16.25	4.549	8.124	19.50	0.15
Ra8Re3.5	3162	10^8	10	10.58	4.762	5.292	8.467	0.05
Ra8Re4	10000	10^8	1	21.08	7.377	10.54	50.58	0.15
Ra8Re4.5	31623	10^8	0.1	49.53	17.33	24.76	118.9	0.15
Ra9Re4	10000	10^9	10	14.12	8.132	7.059	22.59	0.05
Ra9Re4.5	31623	10^9	1	28.63	12.83	14.31	137.4	0.15
Ra9Re5	100000	10^9	0.1	68.13	30.52	34.06	327.0	0.15
Ra10Re4.5	31623	10^{10}	10	27.04	15.88	13.52	38.02	0.03
Ra10Re5	100000	10^{10}	1	54.42	27.21	27.21	255.1	0.10
Ra10Re5.5	316228	10^{10}	0.1	128.0	63.99	63.99	599.9	0.10

Table 2. Grid resolutions for the various flow cases. Here, $\Delta x^+ = u_\tau\Delta x/\nu$, $\Delta y^+_{\mathrm{int}} = u_\tau\Delta y_{\mathrm{int}}/\nu$, $\Delta z^+ = u_\tau\Delta z/\nu$ and $y_p^+ = u_\tau y_p/\nu$ use the statistical friction velocity from the heated lower wall. The interior spacing Δy_{int} is the uniform wall-normal cell spacing, whereas the thickness of each wall-adjacent cell is $2y_p$. Here, y_p is the distance from the corresponding wall boundary face to the centroid of the wall-adjacent control volume. The wall-adjacent cell centres form the wall-model sampling plane. The notation RaXReY denotes configurations with $Ra = 10^{\mathrm{X}}$ and $Re_b = 10^{\mathrm{Y}}$.

To couple momentum and heat transfer at the wall, the model uses the instantaneous quantities averaged over the sampling plane in a separate iterative solve for each wall at each time step. Specifically, at the lower wall we define

$$U_p(t) = \langle u_x(x, y_p, z, t)\rangle_{x,z}, \qquad T_p(t) = \langle T(x, y_p, z, t)\rangle_{x,z},$$

where $\langle\cdot\rangle_{x,z}$ denotes an instantaneous plane average. At the upper wall, the corresponding sampling-plane quantities are evaluated at $y = 2h - y_p$. For each wall, the iteration determines scalar coefficients $\nu_{t,w}(t)$ and $\alpha_{t,w}(t)$, which are spatially uniform over that wall patch. The corresponding total effective viscosity and thermal diffusivity include the molecular contributions, namely, $\nu_{\text{eff},w}(t) = \nu + \nu_{t,w}(t)$ and $\alpha_{\text{eff},w}(t) = \alpha + \alpha_{t,w}(t)$. Given an initial estimate of $\nu_{t,w}(t)$, we obtain the corresponding thermal contribution as $\alpha_{t,w}(t) = \nu_{t,w}(t)/Pr_{t,\text{wall}}$ and evaluate the instantaneous plane-averaged wall-model Nusselt number as

$$Nu_w(t) = \frac{2h}{\Delta T}\left(\frac{\alpha_{\text{eff},w}(t)}{\alpha}\right)\frac{|T_w - T_p(t)|}{y_p}, \tag{3.5}$$

where $T_w = T_h$ on the lower wall and $T_w = T_c$ on the upper wall. The corresponding instantaneous plane-averaged wall heat-flux magnitude is $q_w(t) = k\Delta T Nu_w(t)/(2h)$. The resulting $Nu_w(t)$ enters the momentum wall law through $\beta(t) = -Nu_w(t)/(2Re_\tau(t))$, thereby coupling the thermal and momentum wall treatments. The instantaneous friction velocity is evaluated from the corresponding plane-averaged streamwise wall-shear-stress magnitude as $u_\tau(t) = \sqrt{|\tau_w(t)|/\rho}$, and the corresponding friction Reynolds number is $Re_\tau(t) = hu_\tau(t)/\nu$.

The logarithmic-quadratic wall law in equation (2.13) is then solved using the Newton–Raphson method for the dimensionless sampling height $y_p^+(t) = u_\tau(t)y_p/\nu$, whose converged value gives an updated $\nu_{t,w}(t)$. The thermal update and Newton–Raphson solve are repeated until the relative change in $\nu_{t,w}(t)$ is below 1%. After convergence, the final thermal contribution $\alpha_{t,w}(t)$ is obtained from the converged $\nu_{t,w}(t)$ using the prescribed constant $Pr_{t,\text{wall}}$. The converged scalar coefficients $\nu_{t,w}(t)$ and $\alpha_{t,w}(t)$ are applied uniformly over the corresponding wall patch. The velocity satisfies a no-slip condition and the wall temperature is prescribed by a fixed-value condition. In the OpenFOAM implementation, the turbulent viscosity is supplied through the custom `nutPRBWallFunction`, and the turbulent thermal diffusivity is treated using the corresponding thermal wall-function boundary condition. When the momentum and temperature equations are advanced, the local wall-face momentum and heat fluxes are evaluated using these uniform wall coefficients together with the local velocity and temperature gradients. The same scalar effective viscosity $\nu_{\text{eff},w}(t)$ acts on both tangential velocity components through the viscous term. The lower and upper walls are treated independently, so their instantaneous wall coefficients and plane-averaged wall fluxes may differ and evolve in time.

3.2. *A posteriori validation against DNS*

Figure 9 compares the WMLES mean velocity and temperature profiles with the DNS data of Pirozzoli *et al.* (2017). The available DNS profiles cover the lower half-channel, $0 < y/h < 1$. All DNS–WMLES profile comparisons below are restricted to this range, with the DNS profiles linearly interpolated onto the WMLES cell-centre locations. For each case, the single wall-adjacent WMLES cell-centre value next to the heated lower wall is excluded from the error evaluation. The plane containing these wall-adjacent cell centres serves as the wall-model matching plane. For the mean streamwise velocity U/u_f, mean temperature T^* and the three root-mean-square (r.m.s.) velocity fluctuations, we use the pointwise absolute relative error $\epsilon_\phi(y) = |\phi_{\text{WMLES}}(y) - \phi_{\text{DNS}}(y)|/|\phi_{\text{DNS}}(y)|$, where

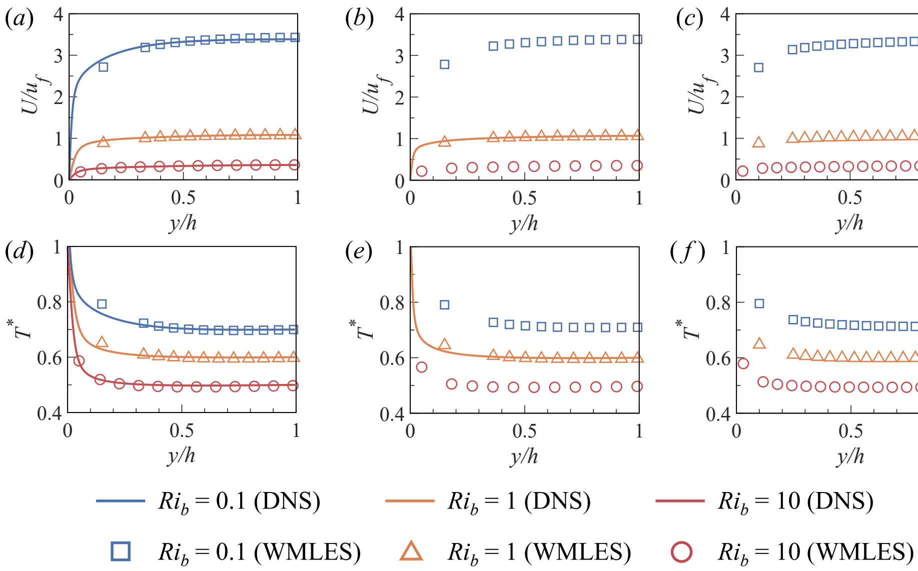

Figure 9. Profiles of (a–c) mean streamwise velocity U/u_f and (d–f) dimensionless mean temperature $T^* = (T - T_c)/\Delta T$ for (a,d) $Ra = 10^8$, (b,e) $Ra = 10^9$, and (c,f) $Ra = 10^{10}$. DNS reference data from Pirozzoli *et al.* (2017) are available for all three Ri_b values (0.1, 1, and 10) at $Ra = 10^8$ in (a,d), and only for $Ri_b = 1$ at $Ra = 10^9$ in (b,e). The remaining profiles, including all $Ra = 10^{10}$ cases in (c,f), are WMLES predictions without corresponding DNS reference data.

ϕ_{WMLES} and ϕ_{DNS} denote the corresponding profiles evaluated at the matched wall-normal locations. Across the DNS-referenced cases shown in figure 9, the maximum pointwise absolute relative errors beyond the wall-model matching plane are 3.6% for the mean streamwise velocity and 1.9% for the mean temperature. The remaining profiles, including all $Ra = 10^{10}$ cases, are predictions of the WMLES framework without corresponding DNS reference data. Across the WMLES cases at fixed Ri_b, the normalised mean-velocity and mean-temperature profiles exhibit only a weak dependence on Ra away from the wall, while more noticeable differences occur in the near-wall region.

We next assess the global heat and momentum transport against the directly matched PRB DNS cases and compare the results with broader external data in figure 10. Across the five directly matched PRB DNS cases listed in table 1, the maximum relative deviations are 11.7% in Nu for Ra7Re3.5 and 15.9% in C_f for Ra8Re4.5. For reference, figure 10(a,b) also includes the empirical correlations proposed by Pirozzoli *et al.* (2017), shown as dotted lines. The correlations for the global Nusselt number and skin-friction coefficient are

$$Nu\,(Ra, Re_b) = \left[\left(0.1165Ra^{0.304}\right)^3 + \left(0.0073Re_b^{0.802}\right)^3\right]^{1/3}, \tag{3.6}$$

and

$$C_f\,(Ra, Re_b) = C_f\,(Re_b)\,f\,(Ri_b)\,, \tag{3.7}$$

where $C_f\,(Re_b)$ follows Prandtl's friction law for turbulent channel flow in the form used by Pirozzoli *et al.* (2017),

Ra	10^8	10^9	10^{10}
Nu_R	30.680205	61.826991	129.776364
Re_R	2002.935340	5760.012287	16489.446203
C_R	0.01532	0.01073	0.00787

Table 3. Pure Rayleigh–Bénard reference quantities at $Pr = 1$ used to normalise the data in figure 10. The values of Nu_R and Re_R are taken from the supplementary material of Yerragolam *et al.* (2024).

$$\sqrt{\frac{2}{C_f\,(Re_b)}} = \frac{1}{\kappa}\ln\left(\frac{Re_b}{2}\sqrt{\frac{C_f\,(Re_b)}{2}}\right) + C_0 - \frac{1}{\kappa}, \tag{3.8}$$

where $\kappa = 0.383$ and $C_0 = 4.17$. The term $-1/\kappa$ results from converting the local logarithmic velocity profile to the channel bulk velocity. The buoyancy correction is (Pirozzoli *et al.* 2017)

$$f\,(Ri_b) = (1 + 4.64Ri_b)^{0.26}\,. \tag{3.9}$$

The external DNS data selected for figure 10 comprise the PRB cases Ra8Re3.5, Ra8Re4, Ra8Re4.5 and Ra9Re4.5 of Pirozzoli *et al.* (2017); the PRB cases at $Ra = 10^8$ with $Re_b = 3000$ and 10000 of Yerragolam *et al.* (2024); and the pressure-driven mixed vertical-convection cases at $Ra = 10^8$ with $Re_b = 3160$ and 10000 of Howland *et al.* (2024). The imposed-flow Reynolds numbers reported in the external studies are denoted by Re_b here. The additional data of Yerragolam *et al.* (2024) and Howland *et al.* (2024) are included to provide broader transport-trend comparisons, with the vertical-convection data serving as a cross-configuration reference.

Figures 10(*c*,*d*) show the same data as figures 10(*a*,*b*), respectively, in the normalised forms Nu/Nu_R and C_f/C_R as functions of Re_b/Re_R. The pure Rayleigh–Bénard reference values Nu_R and Re_R are taken from the supplementary material of Yerragolam *et al.* (2024) at the corresponding Ra and Pr. Here, Re_R is the large-scale-circulation Reynolds number estimated from the r.m.s. velocity in the pure-RB state as $Re_R = U_{\rm rms}H/\nu$, where $H = 2h$ is the full height of the RB cell. The reference coefficient C_R estimates the response friction coefficient associated with the large-scale-circulation rolls in pure RB convection. The heat–momentum transport scaling of Yerragolam *et al.* (2024) is $Nu \sim Pr^{1/3}C_TRe_T$, where Re_T and C_T characterise the total flow. For consistency with the normalisation used in figure 3(d) of Yerragolam *et al.* (2024), we take the pure-RB reference coefficient as $C_R = Nu_R/(Re_RPr^{1/3})$. The numerical reference values used at $Pr = 1$ are listed in table 3.

For consistency across configurations, the vertical-convection data of Howland *et al.* (2024) are normalised using the same pure-RB reference quantities Nu_R, Re_R and C_R at the corresponding Ra, rather than using pure vertical-convection reference values. This common normalisation is used to facilitate comparison of transport responses across the different mixed-convection configurations. To interpret these normalised results, we consider the limiting relations proposed by Yerragolam *et al.* (2024). In their general notation, Re_S and C_S characterise the externally imposed shear; for the present PRB configuration, they correspond to Re_b and C_f, respectively. In the buoyancy-dominated regime, the normalised heat transfer is described by

$$\frac{Nu}{Nu_R} = \left[1 + \left(\frac{Re_b}{Re_R}\right)^2\right]^{-1/10}. \tag{3.10}$$

Following the reference curve used in figure 3(d) of Yerragolam *et al.* (2024), the buoyancy-dominated friction scaling is represented as

$$\frac{C_f}{C_R} = 2.5\frac{Re_R}{Re_b}. \tag{3.11}$$

In the strong-shear limit, Yerragolam *et al.* (2024) express the friction coefficient as

$$\sqrt{\frac{2}{C_f}} = \frac{1}{\kappa_Y}\ln\left(Re_b\sqrt{\frac{C_f}{8}}\right) + B_Y, \tag{3.12}$$

where $\kappa_Y = 0.41$ and $B_Y = 5$. Here, B_Y denotes the additive constant in the friction relation and is distinct from the log-law intercept C_0 used in equation (3.8). The corresponding heat-transfer relation is

$$Nu = 0.25Pr^{1/2}C_fRe_b. \tag{3.13}$$

The black dashed lines in figures 10(*c*,*d*) represent the buoyancy-dominated relations (3.10) and (3.11), respectively, whereas the coloured dashed lines represent the corresponding strong-shear relations (3.13) and (3.12), respectively. The relations are normalised separately using the reference values at each Ra. Although quantitative deviations remain in the transitional region, the two limiting descriptions capture the overall changes in heat transport and wall friction within their respective regimes.

Figure 11 shows WMLES second-order statistics computed from the resolved velocity and temperature fields. The DNS profiles of Pirozzoli *et al.* (2017) are used as unfiltered reference statistics. Figures 11(*a*–*c*) compare the r.m.s. velocity fluctuations as functions of wall-normal position at $Ri_b = 1$. Across the DNS-referenced cases shown in figure 11, the maximum pointwise absolute relative errors in u'_{rms}, v'_{rms} and w'_{rms} are 7.77%, 9.86% and 13.86%, respectively. Figures 11(*d*,*e*) compare the resolved Reynolds shear stress $-\langle u'v'\rangle_{x,z,t}$ and resolved wall-normal turbulent heat flux $\langle v'T'\rangle_{x,z,t}$ from WMLES with the corresponding unfiltered DNS turbulent moments. Because the DNS Reynolds shear stress approaches zero near the centreline, we assess both transport profiles using the peak-DNS-normalised absolute error, defined as $\epsilon_{\phi,N}(y) = |\phi_{\mathrm{WMLES}}(y) - \phi_{\mathrm{DNS}}(y)|/\max_y|\phi_{\mathrm{DNS}}(y)|$, where ϕ denotes either of these transport quantities, and the denominator is the peak magnitude of the corresponding DNS reference profile in the lower half-channel. The same lower-half-channel restriction, linear interpolation and exclusion of each case's wall-adjacent cell-centre value apply to the evaluation of both error profiles. The maximum peak-DNS-normalised absolute errors across the two DNS-referenced cases are 7.7% for the resolved Reynolds shear stress and 16.4% for the resolved wall-normal turbulent heat flux. The near-wall peaks in the resolved Reynolds shear stress are under-resolved on the coarse mesh, whereas the resolved wall-normal turbulent heat flux is underpredicted in the bulk region, particularly at $Ra = 10^9$. We also evaluated the modelled SGS contribution to the wall-normal heat flux. Away from the wall-adjacent cell, this contribution is less than approximately 1% of the total turbulent heat flux, and adding it produces no material change in the comparison with DNS. The bulk-region discrepancy at $Ra = 10^9$ therefore cannot be attributed to omission of the modelled SGS flux from figure 11(*e*), but instead

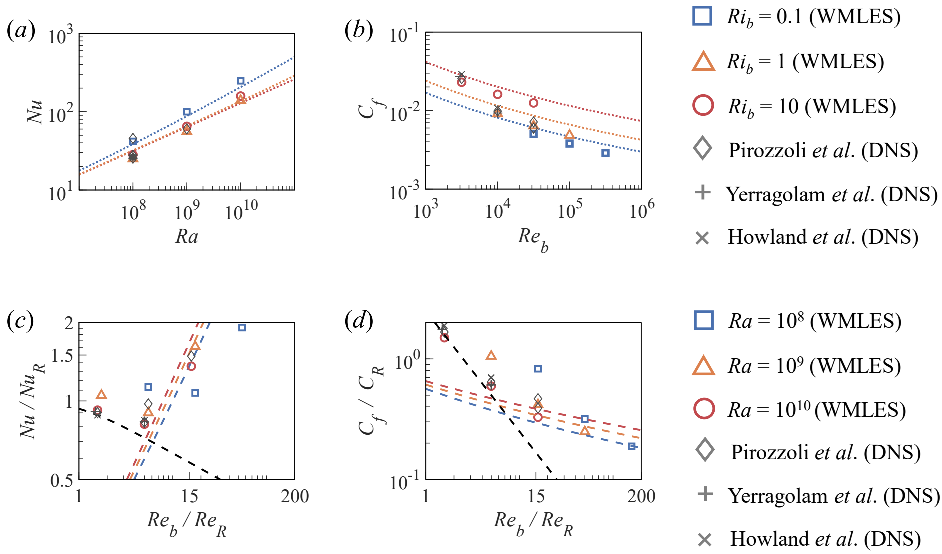

Figure 10. Variation of (*a*) global Nusselt number Nu with Rayleigh number Ra, and (*b*) friction coefficient C_f with bulk Reynolds number Re_b. (*c*) and (*d*) show the same data as (*a*) and (*b*), respectively, normalised by the corresponding pure Rayleigh–Bénard reference values Nu_R, C_R and Re_R in table 3. Grey symbols show the selected $Pr = 1$ DNS data from Pirozzoli *et al.* (2017), Yerragolam *et al.* (2024), and Howland *et al.* (2024); the case selection is specified in the text. In (*a*,*b*), the dotted lines denote the empirical correlations of Pirozzoli *et al.* (2017). In (*c*,*d*), the black dashed lines show the buoyancy-dominated predictions of Yerragolam *et al.* (2024), while the coloured dashed lines show the corresponding strong-shear predictions evaluated separately at each Ra.

reflects limitations of the present WALE-based LES treatment and resolution for turbulent thermal transport.

To assess how the WMLES distributes energy across spatial scales, we then compare the spanwise spectra at the channel centreline with the DNS data of Pirozzoli *et al.* (2017). As shown in figure 12, the WMLES reproduces the pronounced spectral peak of the streamwise-velocity fluctuations around $\lambda_z/h \approx 4$ for all three bulk Richardson numbers, although some differences in peak magnitude remain. For the wall-normal velocity and temperature, both the DNS and WMLES spectra generally increase towards the longest resolved spanwise wavelengths, indicating appreciable contributions from large spanwise scales. The WMLES captures these overall spectral trends, but quantitative discrepancies become more evident at the largest resolved wavelength, $\lambda_z/h = 8$, particularly for the wall-normal velocity and temperature spectra. Thus, the dominant spanwise scale of the streamwise-velocity fluctuations is reproduced more closely than the spectral amplitudes of the large-scale wall-normal-velocity and temperature fluctuations.

3.3. *Mesh-count reduction and DNS extrapolation*

To quantify the reduction in mesh count, we compare the DNS meshes used by Pirozzoli *et al.* (2017) with the present WMLES meshes in figure 13. Over $10^7 \leq Ra \leq 10^9$, the WMLES achieves reductions in mesh count by factors of approximately 195–542 relative to the corresponding DNS meshes. For the $Ra = 10^{10}$ and $Ri_b = 0.1$ case ($Re_\tau \approx 6000$), no corresponding PRB DNS is presently available. We therefore estimate a reference DNS mesh count using shear-driven channel-flow and buoyancy-driven convection scalings.

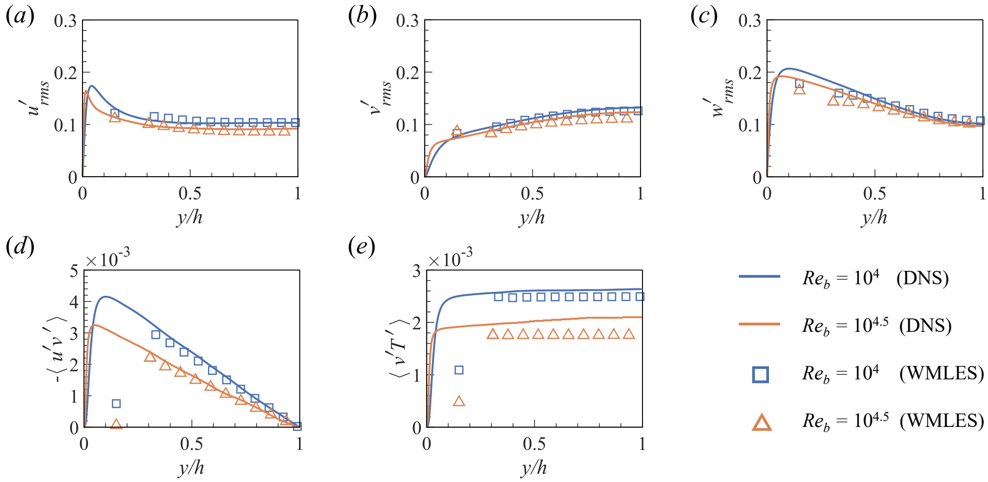

Figure 11. Wall-normal profiles of the second-order turbulent statistics for $(Ra, Re_b) = (10^8, 10^4)$ and $(10^9, 10^{4.5})$ at $Ri_b = 1$. All WMLES statistics are computed from the resolved velocity and temperature fields and are compared with the unfiltered DNS reference statistics of Pirozzoli *et al.* (2017). (*a–c*) r.m.s. velocity fluctuations u'_{rms}, v'_{rms}, and w'_{rms}, respectively; (*d*) resolved Reynolds shear stress $-\langle u'v' \rangle_{x,z,t}$; (*e*) resolved wall-normal turbulent heat flux $\langle v'T' \rangle_{x,z,t}$. The r.m.s. velocity fluctuations are normalised by u_f, the Reynolds shear stress by u_f^2, and the turbulent heat flux by $u_f \Delta T$.

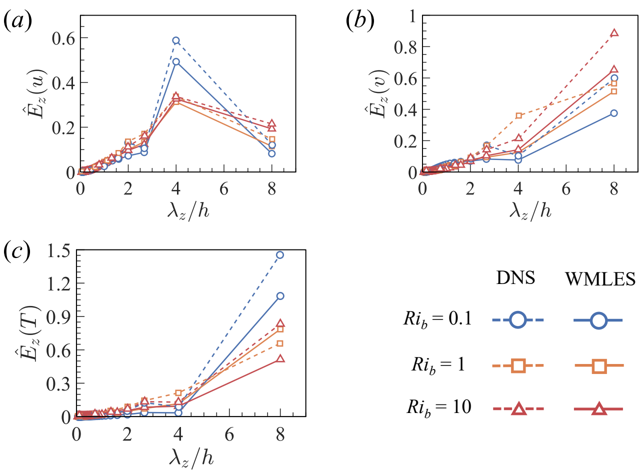

Figure 12. Nondimensional spanwise spectral densities at the channel centreline. Normalised spectra of (*a*) streamwise velocity, (*b*) wall-normal velocity, and (*c*) temperature as functions of spanwise wavelength at $Ra = 10^8$. Each spectrum is normalised by the variance of the corresponding quantity.

For the shear-driven limit, a fixed domain in outer units and approximately constant streamwise and spanwise resolution in wall units give $N_x, N_z \propto Re_\tau$. Following the asymptotic wall-normal grid-point scaling discussed by Pirozzoli & Orlandi (2021), we adopt $N_y \propto Re_\tau^{3/4}$, giving $N_{\mathrm{ch,ext}} \propto Re_\tau^{2.75}$. The mesh count of a reference channel DNS in a domain $L_{x,\mathrm{ref}} \times 2h \times L_{z,\mathrm{ref}}$ is first rescaled to the present $16h \times 2h \times 8h$ domain at fixed spatial resolution and then extrapolated in Re_τ, thus

$$N_{\mathrm{ch,ext}} = N_{\mathrm{ref}} \frac{16h}{L_{x,\mathrm{ref}}} \frac{8h}{L_{z,\mathrm{ref}}} \left(\frac{Re_{\tau,\mathrm{target}}}{Re_{\tau,\mathrm{ref}}} \right)^{2.75}, \tag{3.14}$$

where $Re_{\tau,\mathrm{target}} = 6000$. The CH4 case of Bernardini *et al.* (2014) has $Re_{\tau,\mathrm{ref}} = 4079$, a domain of $6\pi h \times 2h \times 2\pi h$, and a mesh of $8192 \times 1024 \times 4096$. The LM5200 case of Lee & Moser (2015) has $Re_{\tau,\mathrm{ref}} = 5186$, a domain of $8\pi h \times 2h \times 3\pi h$, and a published discretisation count of $10240 \times 1536 \times 7680$. For this spectral DNS, the published streamwise and spanwise counts denote numbers of Fourier modes, and the wall-normal count denotes the number of B-spline basis functions. Applying equation (3.14) to the unrounded mesh products and domain factors gives $N^{\mathrm{CH4}}_{\mathrm{ch,ext}} \approx 1.073 \times 10^{11}$ and $N^{\mathrm{LM5200}}_{\mathrm{ch,ext}} \approx 9.747 \times 10^{10}$; thus, the shear-driven estimate is $N_{\mathrm{ch,ext}} \approx (9.7\text{–}10.7) \times 10^{10}$.

For the buoyancy-based extrapolation, the bulk-resolution criterion of Grötzbach (1983) is

$$\frac{\varDelta_{\mathrm{char}}}{H} \lesssim \pi \left(\frac{Pr^2}{Ra\, Nu_R} \right)^{1/4}, \tag{3.15}$$

where $H = 2h$ and $\varDelta_{\mathrm{char}}$ denotes a characteristic bulk spacing. At fixed $Pr = 1$, this gives $\varDelta_{\mathrm{char}}/H \propto [Ra\, Nu_R(Ra)]^{-1/4}$, so the reference Nusselt numbers can determine the change in resolution scale without requiring an additional power-law fit. We use the pure-RB Nusselt numbers at $Pr = 1$ reported by Yerragolam *et al.* (2024), consistent with the reference data in table 3.

We anchor the extrapolation to the $Ra = 10^9$ reference grid of Pirozzoli *et al.* (2017), $N_{\mathrm{ref}} = 6144 \times 768 \times 3072 \approx 1.45 \times 10^{10}$, used for both pure-RB and PRB cases in the same $16h \times 2h \times 8h$ domain. Assuming that the domain remains fixed and that all three directions are refined by the same factor implied by the characteristic bulk scale gives

$$N_{\mathrm{buoy,ext}} = N_{\mathrm{ref}} \left[\frac{Ra_{\mathrm{target}} Nu_R(Ra_{\mathrm{target}})}{Ra_{\mathrm{ref}} Nu_R(Ra_{\mathrm{ref}})} \right]^{3/4}. \tag{3.16}$$

Using $Ra_{\mathrm{ref}} = 10^9$, $Ra_{\mathrm{target}} = 10^{10}$ and the corresponding pure-RB Nusselt numbers in table 3 gives $N_{\mathrm{buoy,ext}} \approx 1.42 \times 10^{11}$. We adopt the larger of the shear-driven and buoyancy-driven estimates as $N_{\mathrm{DNS,ext}} = \max\left(N_{\mathrm{ch,ext}}, N_{\mathrm{buoy,ext}}\right) \approx 1.42 \times 10^{11}$. The present WMLES mesh contains $750 \times 152 \times 750 = 8.55 \times 10^7$ cells, giving an extrapolated DNS-to-WMLES mesh-count ratio of approximately 1660.

3.4. *Sensitivity to wall-model parameters*

We quantify the sensitivity of the WMLES to the prescribed wall-model parameters using case Ra8Re4 as the baseline. We perturb C by ±10% and $Pr_{t,\mathrm{wall}}$ by ±30% about their baseline values of 0.9. The mean velocity and global transport are sensitive to C, as shown in figure 14(*a*) and table 4. With $C = 0.81$, Re_τ and Nu are underpredicted relative to DNS by approximately 39% and 61%; with $C = 0.99$, they are overpredicted by approximately 25% and 67%, respectively. Thus, the calibration of C, which affects both the offset and the logarithmic slope of the wall law, has a substantial effect on the predicted transport. Perturbing $Pr_{t,\mathrm{wall}}$ by ±30% produces smaller changes in the mean-velocity profiles than perturbing C by ±10% (figure 14). Relative to DNS, the resulting signed relative errors range from −13.38% to +11.26% in Re_τ and from −21.66% to +33.67% in Nu, as reported in table 4. The calibrated values of C are retained for the investigated Ri_b cases. The strong transport response to perturbations of C indicates that extrapolation to higher Ra

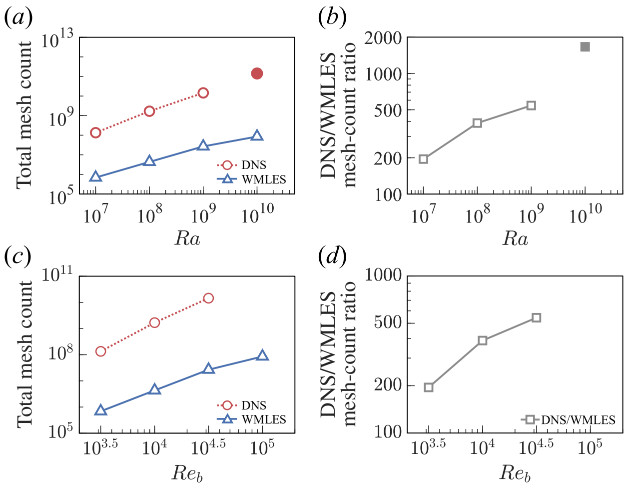

Figure 13. Comparison of DNS and WMLES mesh counts. (*a*) Total mesh count versus Ra. (*b*) DNS-to-WMLES mesh-count ratio versus Ra. (*c*) Total mesh count versus Re_b at $Ri_b = 1$. (*d*) DNS-to-WMLES mesh-count ratio versus Re_b. Open circles denote available DNS mesh counts, open triangles the present WMLES mesh counts, and open squares ratios based on available DNS meshes. The filled circle in (*a*) and filled square in (*b*) denote the selected extrapolated DNS mesh count and the corresponding ratio for the $Ra = 10^{10}$, $Ri_b = 0.1$, $Re_\tau \approx 6000$ case. (*c*,*d*) are restricted to the $Ri_b = 1$ sequence and do not include this estimate.

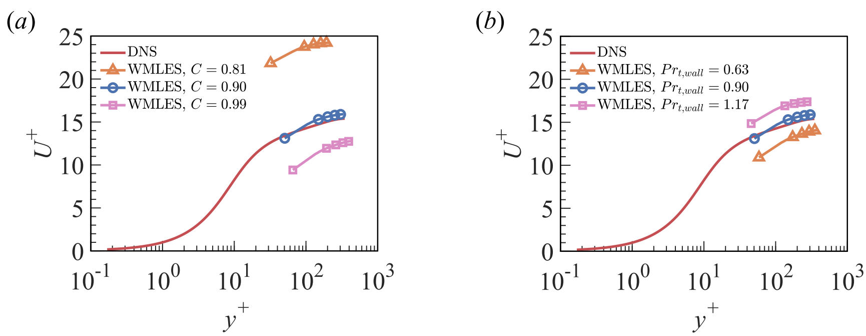

Figure 14. Sensitivity of the mean streamwise velocity profiles to variations in the wall-model parameters for case Ra8Re4 ($Ra = 10^8$, $Re_b = 10^4$). (*a*) Effect of perturbing the rescaled integration parameter C by ±10% around its baseline value of 0.9. (*b*) Effect of perturbing the wall turbulent Prandtl number $Pr_{t,\mathrm{wall}}$ by ±30% around its baseline value of 0.9. The solid red lines denote DNS data from Pirozzoli *et al.* (2017).

remains sensitive to uncertainty in this parameter. This sensitivity motivates quantifying the calibration uncertainty in C and developing a predictive closure to replace regime-dependent calibration, potentially incorporating non-equilibrium near-wall effects. Recent knowledge-integrated approaches combine reduced near-wall physics with data-assisted corrections for effects not represented by equilibrium wall laws (Zhang *et al.* 2025), and differentiable WMLES provides a framework for in situ learning and optimisation of wall models using limited reference data (Zhang *et al.* 2026).

Flow case	$Pr_{t,\mathrm{wall}}$	C	Nu (ϵ_r)	Re_τ (ϵ_r)
Ra8Re4-DNS	-	-	25.443	351.01
Ra8Re4-WMLES	0.9	0.9	25.053 (−1.53%)	337.22 (−3.93%)
Ra8Re4-WMLES	0.9	0.81	9.8088 (−61.45%)	214.12 (−39.00%)
Ra8Re4-WMLES	0.9	0.99	42.523 (+67.13%)	437.31 (+24.59%)
Ra8Re4-WMLES	0.63	0.9	34.009 (+33.67%)	390.53 (+11.26%)
Ra8Re4-WMLES	1.17	0.9	19.932 (−21.66%)	304.05 (−13.38%)

Table 4. Sensitivity of the predicted global flow statistics Nu and Re_τ to variations in the wall-model parameters. The baseline case is Ra8Re4 ($Ra = 10^8$, $Re_b = 10^4$), for which the baseline parameters are $C = 0.9$ and $Pr_{t,\mathrm{wall}} = 0.9$. The rescaled integration parameter C is perturbed by ±10%, whereas the wall turbulent Prandtl number $Pr_{t,\mathrm{wall}}$ is perturbed by ±30%. DNS data from Pirozzoli *et al.* (2017) are included for comparison. The parenthesised values are signed relative errors $\epsilon_r = [\phi_{\mathrm{WMLES}} - \phi_{\mathrm{DNS}}]/\phi_{\mathrm{DNS}}$, expressed as percentages, for $\phi = Nu$ or Re_τ.

4. Modulation of turbulent structures by shear and buoyancy

4.1. *Instantaneous flow organisation across regimes*

We first examine how the instantaneous flow organisation changes with the relative importance of shear and buoyancy. Figures 15–17 show contours of streamwise velocity, wall-normal velocity and temperature at the channel mid-plane ($y/h = 1$) for the three Ri_b regimes. The panels compare cases along each fixed-Ri_b sequence, in which Ra, Re_b and Re_τ increase together while the global ratio of buoyancy to shear remains fixed. Complementary three-dimensional temporal visualisations are provided in supplementary movies 1–3, showing instantaneous Q-criterion isosurfaces coloured by temperature, volume renderings of the streamwise velocity, and volume renderings of the temperature field, respectively. The movies compare the three Ri_b regimes at $Ra = 10^{10}$ and the three Rayleigh numbers along the fixed-$Ri_b = 1$ sequence. When shear dominates ($Ri_b = 0.1$; figure 15), the streamwise-velocity and temperature structures remain predominantly elongated in the streamwise direction. This common alignment is consistent with the influence of streamwise shear on the organisation of both the velocity and temperature fields. When shear and buoyancy are comparable ($Ri_b = 1$; figure 16), the velocity and temperature streaks remain predominantly streamwise but become less spatially continuous, consistent with the DNS observations of Pirozzoli *et al.* (2017). Along the fixed-$Ri_b = 10$ sequence (figure 17), the streamwise-velocity field changes from fragmented patterns at $Ra = 10^8$ and 10^9 to broader regions at $Ra = 10^{10}$, while the wall-normal velocity and temperature fields retain organised spatial features. We quantify this change below using the streamwise threshold correlation length and the low-wavenumber spectral contribution.

4.2. *Full-field POD and modal energy distribution*

The instantaneous contours provide a qualitative picture of the large-scale flow organisation. To identify its dominant energetic components and quantify their relative contributions, we apply full-field proper orthogonal decomposition (POD) to the three-component instantaneous velocity field $\boldsymbol{u} = (u, v, w)$. POD has been used to characterise large-scale circulations in convection cells (Castillo-Castellanos *et al.* 2019; Soucasse *et al.* 2019). The full velocity field is decomposed into spatial POD modes $\boldsymbol{\varphi}_i(\boldsymbol{x})$ and temporal coefficients $a_i(t)$:

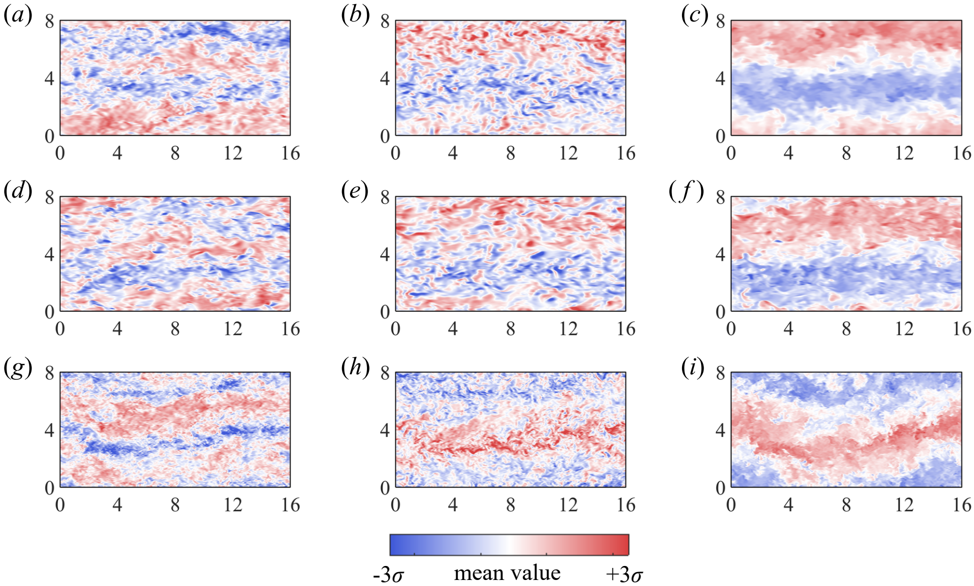

Figure 15. Instantaneous contours at mid-height for Ri_b = 0.1: (*a*,*d*,*g*) streamwise velocity, (*b*,*e*,*h*) wall-normal velocity, and (*c*,*f*,*i*) temperature. (*a*–*c*) $Ra = 10^8$, (*d*–*f*) $Ra = 10^9$, (*g*–*i*) $Ra = 10^{10}$. For each variable, contours are shown within ±3 standard deviations of the mean.

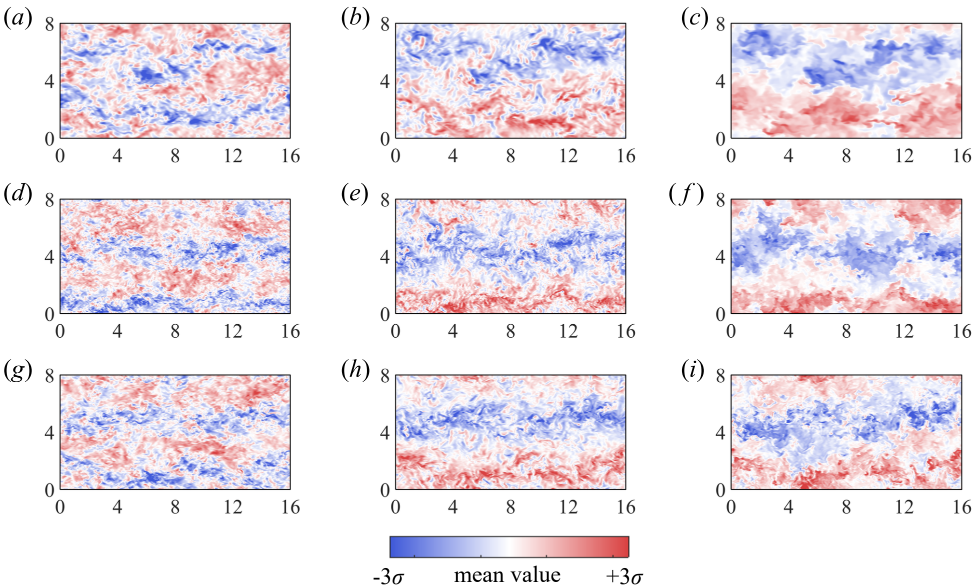

Figure 16. Instantaneous contours at mid-height for Ri_b = 1: (*a*,*d*,*g*) streamwise velocity, (*b*,*e*,*h*) wall-normal velocity, and (*c*,*f*,*i*) temperature. (*a*–*c*) $Ra = 10^8$, (*d*–*f*) $Ra = 10^9$, (*g*–*i*) $Ra = 10^{10}$. For each variable, contours are shown within ±3 standard deviations of the mean.

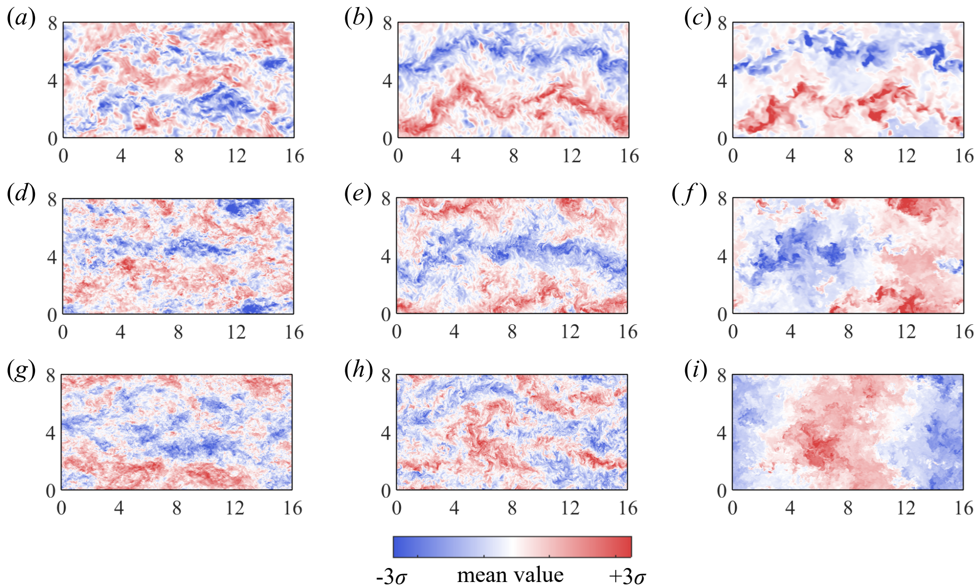

Figure 17. Instantaneous contours at mid-height for $Ri_b = 10$: (*a*,*d*,*g*) streamwise velocity, (*b*,*e*,*h*) wall-normal velocity, and (*c*,*f*,*i*) temperature. (*a*–*c*) $Ra = 10^8$, (*d*–*f*) $Ra = 10^9$, (*g*–*i*) $Ra = 10^{10}$. For each variable, contours are shown within ±3 standard deviations of the mean.

$$\boldsymbol{u}(\boldsymbol{x}, t) = \sum_{i=1}^{\infty} a_i(t)\boldsymbol{\varphi}_i(\boldsymbol{x}). \tag{4.1}$$

The temporal coefficients satisfy

$$\langle a_i(t)a_j(t)\rangle_t = \delta_{ij}\lambda_i, \tag{4.2}$$

where δ_{ij} is the Kronecker delta and $\langle\cdot\rangle_t$ denotes temporal averaging. The eigenvalues λ_i measure the modal contributions to the full-field kinetic energy, and $\lambda_i/\sum_j \lambda_j$ gives the fraction contained in mode i. Figure 18 shows the wall-normal component of the leading full-field POD mode. It reveals a streamwise-oriented roll-like organisation in all cases. This shared modal pattern indicates that coherent roll-like organisation remains identifiable even when the instantaneous streamwise-velocity patterns become more fragmented.

To quantify the modal energy distribution of the full velocity field, we compare the normalised POD eigenvalues $\lambda_i/\sum_j \lambda_j$ across the three flow regimes in figure 19. At $Ri_b = 0.1$ and 1, the leading mode accounts for more than 95% of the full-field kinetic energy, largely reflecting the contribution of the mean streamwise flow. At $Ri_b = 10$, this fraction decreases to approximately 80%, with a larger fraction distributed among the higher-order modes. Because the temporal mean is retained in the full-field POD, these modal energy fractions include the mean-flow contribution and should not be interpreted as the kinetic-energy fractions of the roll motions alone.

The observed roll-like organisation is consistent with the large-scale rolls discussed in the linear-instability analysis of the turbulent mean flow by Cossu (2022). Cossu (2022) argued that the critical Rayleigh number Ra_c for the onset of this linear instability increases with the bulk Reynolds number Re_b according to $Ra_c \approx 0.04Re_b^{1.8}$. Figure 20 compares this fit with two sampled cases without coherent rolls and the corresponding cases with rolls

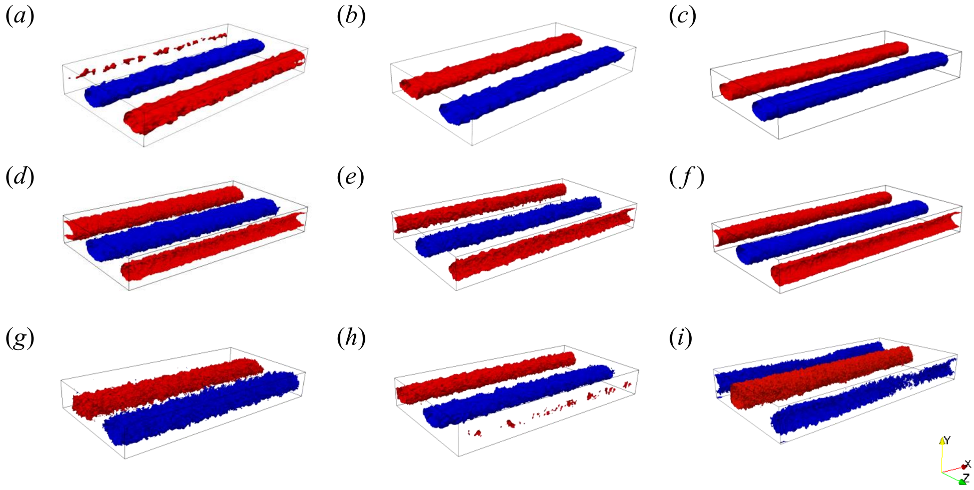

Figure 18. Isosurfaces of the wall-normal component of the leading full-field POD mode, for (*a–c*) $Ra = 10^8$, (*d–f*) $Ra = 10^9$, and (*g–i*) $Ra = 10^{10}$, with (*a,d,g*) $Ri_b = 0.1$, (*b,e,h*) $Ri_b = 1$, and (*c,f,i*) $Ri_b = 10$. The corresponding friction Reynolds numbers are listed in table 1. Red and blue denote positive and negative wall-normal components, respectively.

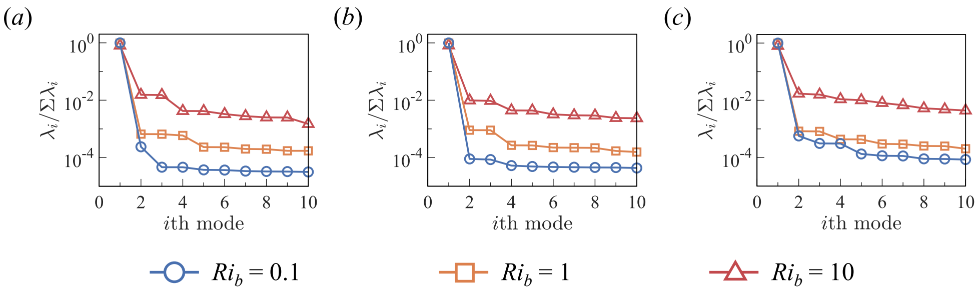

Figure 19. Full-field kinetic-energy fraction $\lambda_i/\sum_j \lambda_j$ contained in each three-component mode of the full-field POD, for (*a*) $Ra = 10^8$, (*b*) $Ra = 10^9$, and (*c*) $Ra = 10^{10}$.

from Pirozzoli *et al.* (2017), together with the present WMLES cases. All present WMLES cases lie above the proposed critical curve and exhibit roll-like structures, consistent with the predicted supercritical organisation. These structures persist up to $Re_b = 10^{5.5}$ in the simulated cases.

4.3. *Correlation lengths and smoothed velocity structures*

We next quantify the spatial extent of the flow structures using two-point correlations of the streamwise-velocity fluctuation $u' = u - \langle u \rangle_{x,z,t}$, where $\langle \cdot \rangle_{x,z,t}$ denotes averaging over the homogeneous streamwise and spanwise directions and the sampling interval. At fixed y/h,

$$R_{uu}(\Delta x, \Delta z; y) = \frac{\langle u'(x,y,z,t)\, u'(x+\Delta x, y, z+\Delta z, t)\rangle_{x,z,t}}{\left\langle u'^2(x,y,z,t)\right\rangle_{x,z,t}}. \tag{4.3}$$

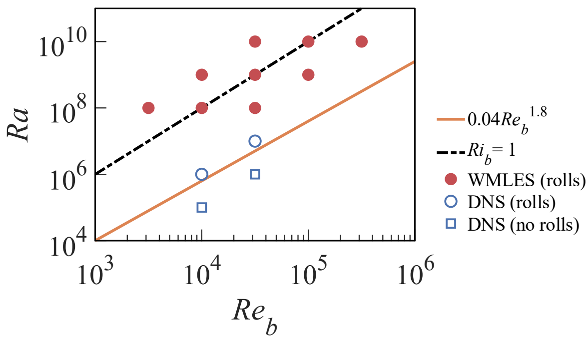

Figure 20. Rayleigh number Ra versus bulk Reynolds number Re_b, showing the predicted critical curve $Ra_c(Re_b)$. The orange solid line is the fit $Ra_c \approx 0.04Re_b^{1.8}$ to the linear-stability predictions of Cossu (2022). Blue open circles and squares denote DNS cases with and without coherent rolls, respectively, from Pirozzoli *et al.* (2017). Red filled circles denote the present WMLES cases, all of which exhibit roll-like structures. The black dashed line denotes $Ri_b = 1$.

The denominator uses the common variance at fixed y, since the two points are separated only in statistically homogeneous directions. One-dimensional correlations are then used to extract threshold correlation lengths. The streamwise and spanwise correlations are obtained by setting $\Delta z = 0$ and $\Delta x = 0$, respectively. The threshold correlation lengths L_x and L_z are defined as the smallest positive separations at which R_{uu} first falls below 0.15. These lengths describe the spatial extent of correlated fluctuations. Figure 21 shows the wall-normal variations of L_x and L_z for different Ri_b. In the shear-dominated regime ($Ri_b = 0.1$, figure 21(*a*,*d*)), L_x is substantially larger than L_z, consistent with elongated shear-driven streak-like motions. Along this fixed-Ri_b path, increasing Ra is accompanied by increasing Re_b and Re_τ, and the streamwise threshold correlation length increases substantially. At $Ra = 10^8$ and 10^9, the lengths are similar to those at $Ri_b = 1$; at $Ra = 10^{10}$, L_x reaches approximately $3h$, whereas L_z increases only moderately. When shear and buoyancy are comparable ($Ri_b = 1$, figure 21(*b*,*e*)), both lengths remain relatively small and vary only weakly along the fixed-Ri_b sequence over $Ra = 10^8$–10^{10}. Under buoyancy-dominated conditions ($Ri_b = 10$, figure 21(*c*,*f*)), both lengths decrease towards the channel centre and vary strongly along the fixed-Ri_b sequence. At $Ra = 10^8$ and 10^9, L_x remains of order h, while L_z decreases from approximately $1.5h$–$2.0h$ near the wall to $0.4h$–$0.6h$ near the centreline. At $Ra = 10^{10}$, L_x reaches approximately $2.0h$–$2.6h$, roughly twice its values at the lower Rayleigh numbers, while L_z decreases from approximately $2.5h$ near the wall to $0.8h$ near the centreline.

To visualise the spatial organisation of the low-speed motions, we apply two-dimensional Gaussian smoothing to the streamwise-velocity fluctuation u' at $y/h = 1$. The Gaussian kernel is defined in physical coordinates as

$$G(x,z) = \frac{1}{2\pi\sigma_x\sigma_z}\exp\left[-\frac{x^2}{2\sigma_x^2} - \frac{z^2}{2\sigma_z^2}\right], \tag{4.4}$$

with fixed physical standard deviations $\sigma_x = h/8$ and $\sigma_z = h/16$ for all cases. The Gaussian filter has a gradual spectral response, and the smoothing highlights spatial organisation without defining a sharp separation between large- and small-scale motions. After truncation at three standard deviations in each direction, the discrete Gaussian kernel is renormalised so that its weights sum to unity. The convolution is performed periodically in the homogeneous streamwise and spanwise directions. We denote the smoothed fluctuation

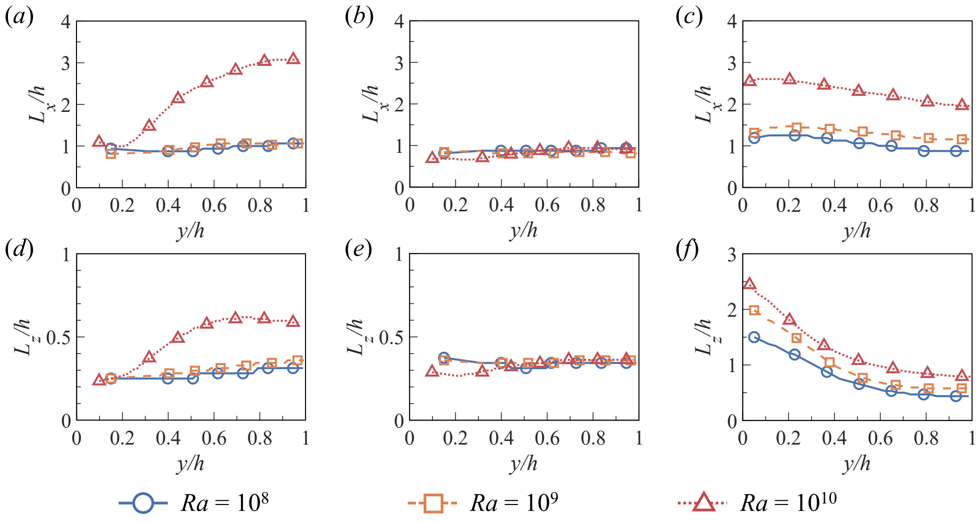

Figure 21. Wall-normal variations of (*a–c*) streamwise threshold correlation length L_x and (*d–f*) spanwise threshold correlation length L_z. (*a*,*d*) $Ri_b = 0.1$, (*b*,*e*) $Ri_b = 1$, and (*c*,*f*) $Ri_b = 10$. The lengths are determined from two-point correlations of streamwise velocity fluctuations using a threshold value of 0.15.

by u'_G and plot negative values of u'_G/u_τ in figure 22. In the shear-dominated regime ($Ri_b = 0.1$), the smoothed low-speed regions become progressively more elongated in the streamwise direction as Ra, Re_b and Re_τ increase along the fixed-Ri_b sequence (figure 22(*a*,*d*,*g*)). This trend is consistent with the pronounced increase in L_x shown in figure 21(*a*). When shear and buoyancy are comparable ($Ri_b = 1$), the smoothed fields remain comparatively fragmented over the investigated range (figure 22(*b*,*e*,*h*)), consistent with the relatively small streamwise and spanwise threshold correlation lengths in figure 21(*b*,*e*). Under buoyancy-dominated conditions ($Ri_b = 10$), the smoothed fields exhibit broader low-speed regions whose organisation changes along the fixed-Ri_b sequence (figure 22(*c*,*f*,*i*)). The particularly pronounced low-speed regions in the highest-Ra case are consistent with the increased threshold correlation lengths above and the low-wavenumber spectral energy discussed below.

4.4. *Spectral signatures of VLSM-like motions and rolls*

To examine whether the $Ri_b = 0.1$ cases exhibit signatures consistent with coexisting VLSM-like streamwise-elongated motions and buoyancy-associated rolls, we compute the two-dimensional premultiplied spectra $k_x k_z E_{xz}(u)\,(\lambda_x, \lambda_z)$ of the streamwise-velocity fluctuations. As shown in figure 23(*a*,*b*), at the lower Rayleigh numbers along the fixed-Ri_b sequence, $Ra = 10^8$ and 10^9, the streamwise fluctuation energy is concentrated mainly at relatively small streamwise and spanwise wavelengths, consistent with the typical footprint of large-scale motions (LSMs). The reference line at $\lambda_x/h = 3$ in figure 23 highlights the extension of the spectrum towards longer streamwise wavelengths. At $Ra = 10^{10}$, the spectrum extends to longer streamwise and spanwise wavelengths (figure 23(*c*)). In particular, appreciable spectral energy appears beyond $\lambda_x/h \approx 3$ and around $\lambda_z/h \approx 4$, indicating simultaneous signatures of streamwise elongation and wide spanwise organisation. Taken together, the large-λ_x signature and the spanwise signature near $\lambda_z/h \approx 4$ are consistent with the coexistence of VLSM-like streamwise-elongated motions and channel-spanning, buoyancy-associated streamwise rolls at $Ra = 10^{10}$.

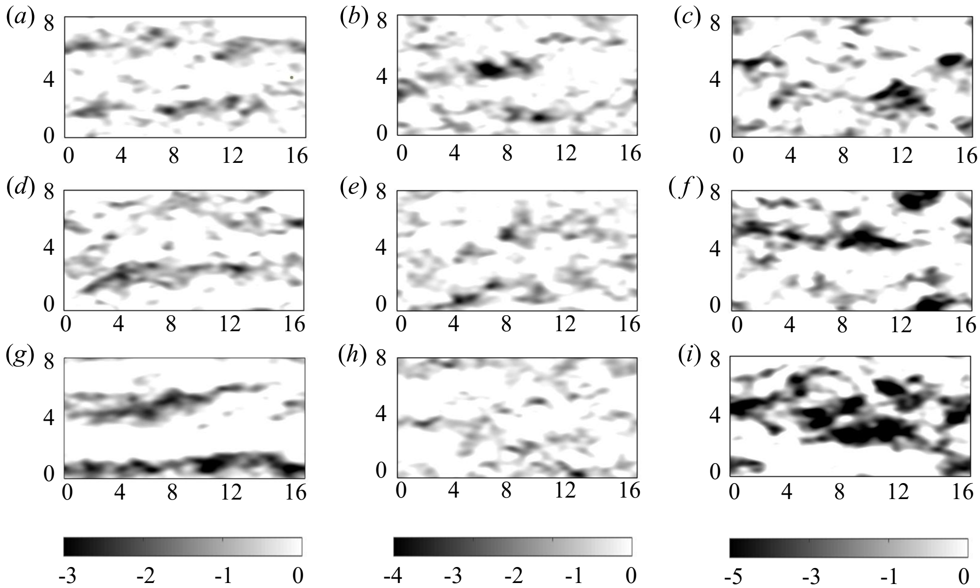

Figure 22. Spatially smoothed streamwise-velocity fluctuations u'_G/u_τ at $y/h = 1$. (*a–c*) $Ra = 10^8$, (*d–f*) $Ra = 10^9$, and (*g–i*) $Ra = 10^{10}$, with (*a,d,g*) $Ri_b = 0.1$, (*b,e,h*) $Ri_b = 1$, and (*c,f,i*) $Ri_b = 10$. Within each fixed-Ri_b column, the same colour limits are used for all three Rayleigh numbers; the limits differ among the three Ri_b values as indicated by the colour bars.

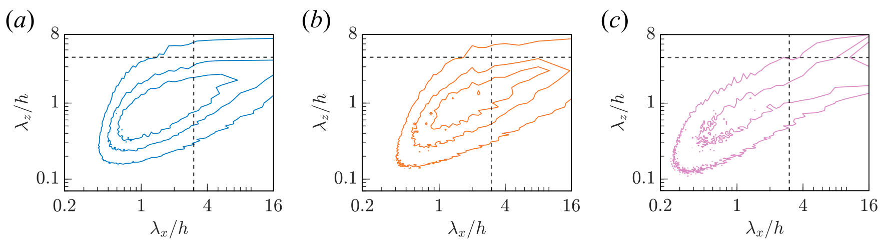

Figure 23. Contours of the two-dimensional premultiplied energy spectra of the streamwise velocity fluctuations at $y/h = 1$, $k_x k_z E_{xz}(u)/u_\tau^2$, as functions of streamwise wavelength λ_x and spanwise wavelength λ_z. (*a*) $Ra = 10^8$, (*b*) $Ra = 10^9$, and (*c*) $Ra = 10^{10}$ for $Ri_b = 0.1$. The black horizontal dashed line marks $\lambda_z/h = 4$, and the black vertical dashed line marks the reference scale $\lambda_x/h = 3$.

At $Ra = 10^{10}$ and $Ri_b = 0.1$, energetic wavelengths approach the streamwise extent of the baseline domain of $L_{\text{box}} = 16h$. We therefore performed an additional calculation in a modified domain $L \times H \times W = 32h \times 2h \times 4h$, with twice the streamwise length and half the spanwise width of the baseline $16h \times 2h \times 8h$ domain. For the visual comparison, we apply the Gaussian smoothing procedure described in §4.3 to the fields in both domains, with $\sigma_x = h/8$ and $\sigma_z = h/16$. The modified domain retains both the long-wavelength spectral contribution and the streamwise-elongated low-speed structures (figure 24(*b*,*d*)). This supports the persistence of the long-wavelength and streamwise-elongated signatures when the streamwise domain length is doubled.

To examine the wall-normal evolution of the spectral contributions, we compare the premultiplied streamwise-velocity spectra at three wall-normal positions in figure 25. When shear dominates or is comparable to buoyancy ($Ri_b = 0.1$ and $Ri_b = 1$; left

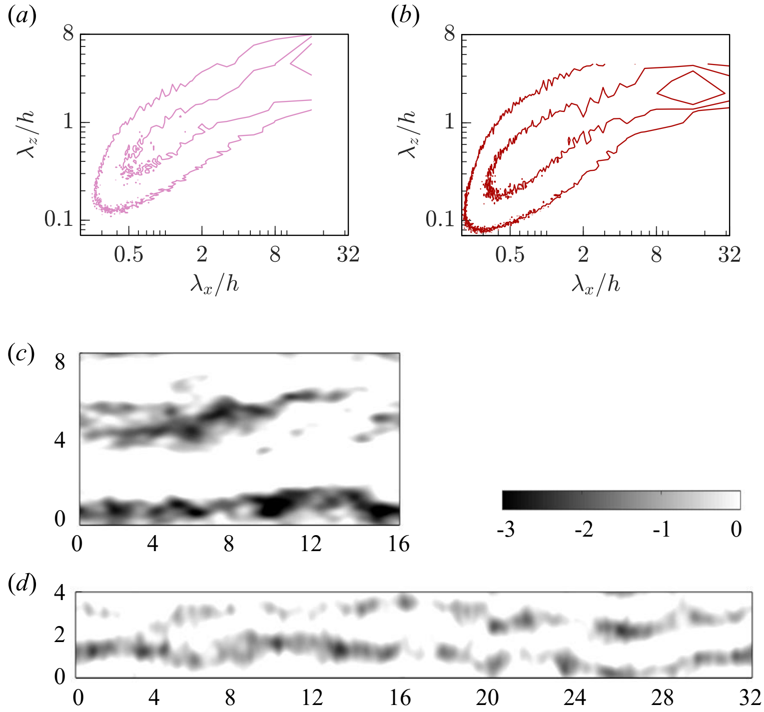

Figure 24. Comparison of the two-dimensional premultiplied energy spectra and spatially smoothed streamwise-velocity fluctuations between the baseline domain ($16h \times 2h \times 8h$) and the modified domain ($32h \times 2h \times 4h$) at $Ra = 10^{10}$ and $Ri_b = 0.1$. (*a*,*c*) Baseline domain; (*b*,*d*) modified domain. (*a*,*b*) Two-dimensional premultiplied spectra $k_x k_z E_{xz}(u)/u_\tau^2$ at $y/h = 1$. (*c*,*d*) Spatially smoothed streamwise-velocity fluctuations u'_G/u_τ at $y/h = 1$. (*c*) shows the same smoothed snapshot as figure 22(*g*). The same colour limits are used in (*c*) and (*d*), matching figure 22(*g*).

and middle columns of figure 25), the spectra generally exhibit a broad maximum at long wavelengths. Where a distinct peak is present, it generally shifts towards shorter streamwise wavelengths with increasing wall-normal distance. At higher Ra, Re_b and Re_τ along the fixed-$Ri_b = 0.1$ sequence (figures 25(*d*,*g*)), the spectral maximum broadens and develops a plateau or shoulder towards larger wavelengths, consistent with the development of VLSM-like long-wavelength contributions. This trend is qualitatively consistent with the long-wavelength spectral behaviour reported in canonical wall turbulence (Kim & Adrian 1999; del Álamo *et al.* 2004). When buoyancy dominates ($Ri_b = 10$; right column of figure 25), the streamwise spectra exhibit a pronounced wall-normal evolution whose detailed form changes along the sequence of increasing Ra, Re_b and Re_τ at fixed Ri_b. At $Ra = 10^8$ and 10^9 (figures 25(*c*,*f*)), a narrow low-wavenumber peak appears near $\lambda_x/h \approx 8$ at the sampling position close to the wall. Its amplitude decreases at $y/h = 0.5$, and the peak becomes substantially weaker and less distinct at the channel centreline. At $Ra = 10^{10}$ (figure 25(*i*)), no isolated peak can be identified near $\lambda_x/h \approx 8$. Instead, at the near-wall and intermediate sampling positions, the spectral energy continues to increase towards the largest wavelength permitted by the computational domain, $\lambda_x/h = 16$, while the centreline spectrum remains elevated at the longest wavelengths. Despite these differences in spectral shape, all three $Ri_b = 10$ cases show that the low-wavenumber contribution to the streamwise-velocity energy is strongest near the wall and

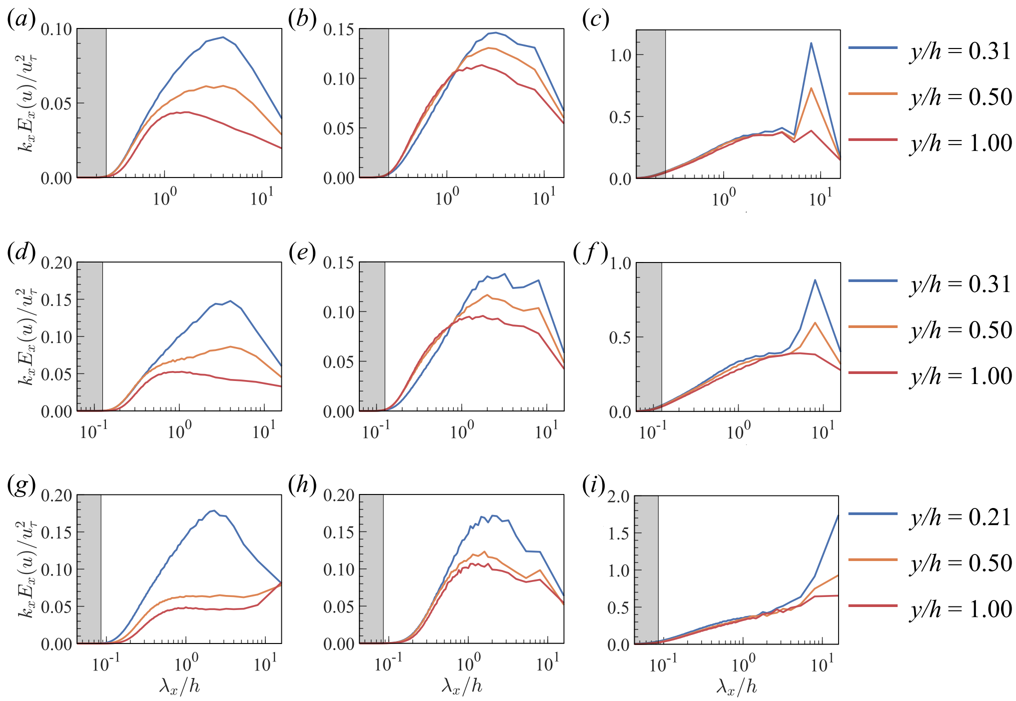

Figure 25. Premultiplied spectra of the streamwise-velocity fluctuation, $k_x E_x(u)/u_\tau^2$, as functions of streamwise wavelength λ_x/h. (*a–c*) $Ra = 10^8$, (*d–f*) $Ra = 10^9$, and (*g–i*) $Ra = 10^{10}$, with (*a,d,g*) $Ri_b = 0.1$, (*b,e,h*) $Ri_b = 1$, and (*c,f,i*) $Ri_b = 10$. The shaded region marks the wavelength range from λ_c to $2\lambda_c$, where $\lambda_c = 2\pi/k_c$ is the corresponding cutoff wavelength and k_c is the maximum streamwise wavenumber resolvable by the grid in each LES case. Spectral data in this range are excluded from the analysis because numerical errors increase near the grid-resolution limit.

weakens towards the channel centreline. This wall-normal attenuation is consistent with a weakening streamwise-velocity imprint of buoyancy-associated roll-like organisation. One interpretation is that wall-normal motions associated with wall-emitted thermal plumes and roll-like organisation redistribute the mean streamwise momentum, generating large-scale streamwise-velocity fluctuations.

5. Conclusion

In this study, we developed and assessed a buoyancy-modified logarithmic-quadratic wall model for WMLES of incompressible PRB flow at $Pr = 1$. The formulation uses a DNS-motivated, approximately linear near-wall relation between the mean temperature and mean streamwise velocity to construct a thermally modified momentum wall law, together with a thermal wall treatment based on a prescribed wall turbulent Prandtl number. The temperature–velocity coefficients match the wall value and the ratio of the wall gradients, while DNS comparisons assess the extension of the resulting wall-matched linear relation to finite distances from the wall. The classical logarithmic law is recovered in the $\beta \rightarrow 0$ asymptotic limit with the corresponding limiting behaviour of C. In the *a priori* comparisons, the three wall-law functional forms are calibrated against DNS; the proposed form gives a closer reconstruction of the near-wall velocity and wall-function-equivalent eddy-viscosity profiles than the implemented Businger–Dyer MOST profile and the model of Scagliarini *et al.* (2015) under strong buoyancy. Across the DNS-referenced cases, the maximum pointwise absolute relative errors beyond the wall-model matching plane are 3.6% in the mean velocity and 1.9% in the mean temperature. Across the cases with available DNS global-transport data, the maximum relative deviations in Nu and C_f are 11.7% and 15.9%, respectively. For cases with corresponding DNS meshes, the reduction factors in mesh count are approximately 195–542. For the $Ra = 10^{10}$ and $Ri_b = 0.1$ case ($Re_\tau \approx 6000$), for which no corresponding PRB DNS data are available, the selected reference-based extrapolation gives a DNS mesh count of approximately 1.42×10^{11}, or 1660 times the present WMLES mesh count. These reductions in mesh requirements extend the accessible range of flow conditions and enable the modal and spectral analyses of large-scale flow organisation at Reynolds and Rayleigh numbers beyond the presently available PRB DNS database.

The simulations also reveal how shear and buoyancy organise the large-scale flow. At $Ri_b = 0.1$, 1 and 10, the wall-normal components of the leading full-field POD modes retain a streamwise-oriented roll-like organisation. In the full-field POD, stronger buoyancy is accompanied by a larger fraction of the modal energy being distributed among higher-order modes. For the $Ra = 10^{10}$, $Ri_b = 0.1$ case, the instantaneous fields, correlation lengths and spectra are consistent with the coexistence of VLSM-like streamwise-elongated motions and buoyancy-associated streamwise rolls. The spectral analysis further reveals distinct wall-normal trends: the long-wavelength contribution remains appreciable into the outer region in the shear-dominated high-Re_τ case, whereas under buoyancy-dominated conditions the low-wavenumber streamwise-velocity contribution is strongest near the wall and weakens towards the channel centre.

The present model relies on regime-dependent calibration, with $C = 0.90$ for the investigated $Ri_b = 0.1$ and 1 cases and $C = 0.95$ for $Ri_b = 10$, based on the available PRB DNS database. The strong sensitivity of the predicted transport to C, together with the absence of DNS reference data and of a dedicated grid-refinement study at $Ra = 10^{10}$, limits confidence in the quantitative accuracy of the highest-Ra predictions. Extending the model to other Richardson or Prandtl numbers and geometries will require further validation and, ultimately, a predictive closure for C and the corresponding thermal wall treatment. Recent Prandtl-number-dependent mean-temperature modelling for incompressible wall turbulence (Sun & Fu 2026) and physics-informed or differentiable wall-model frameworks (Zhang *et al.* 2025, 2026) provide relevant methodological directions. Their extension to buoyancy-coupled active-scalar PRB flow, however, remains to be established.

Supplementary movies Supplementary movies 1–3 are available with the online version of the paper.

Funding. This work was supported by the National Natural Science Foundation of China (NSFC) under grant nos. 12272311, 12388101 and 12125204; the Young Elite Scientists Sponsorship Program by CAST (2023QNRC001); the Fundamental Research Funds for the Central Universities (no. D5000260269); and the 111 project of China (project no. B17037). The authors acknowledge the Computing Center in Xi'an for providing HPC resources that have contributed to the research results reported within this paper.

Declaration of interests. The authors report no conflict of interest.

Author ORCIDs. Ao Xu, https://orcid.org/0000-0003-0648-2701; Heng-Dong Xi, https://orcid.org/0000-0002-2999-2694.

Appendix A. Variations of the pointwise effective parameters

To further examine the use of the rescaled integration parameter C, we compare the pointwise effective parameters $B_{\text{eff}}(y)$ and $C_{\text{eff}}(y)$ at $Ri_b = 1$ for $Ra = 10^6$, 10^7, 10^8 and 10^9. Figures 26(*a*,*b*) show their absolute relative deviations from the corresponding cross-Ra averages, normalised by the magnitudes of those averages.

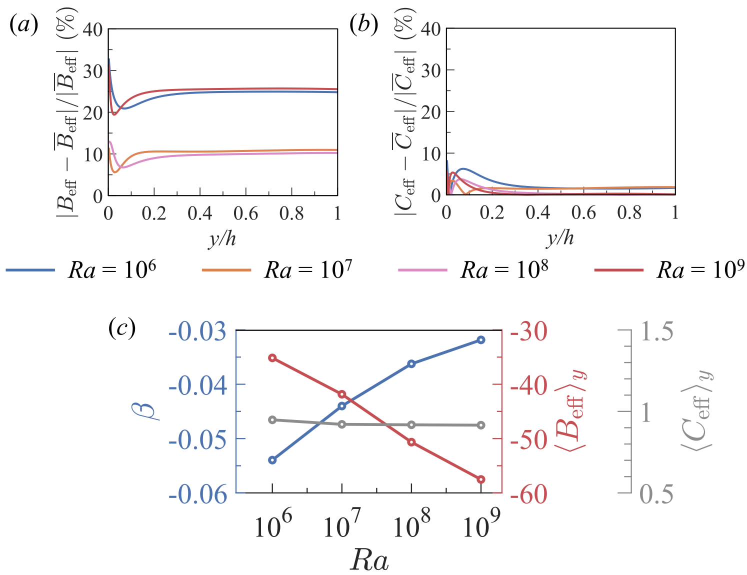

Figure 26. Absolute relative deviations of the pointwise effective parameters (*a*) $B_{\rm eff}(y)$ and (*b*) $C_{\rm eff}(y)$ from their corresponding cross-Ra averages at $Ri_b = 1$, normalised by the magnitudes of those averages and expressed as percentages. The overbar denotes averaging over $Ra = 10^6$, 10^7, 10^8 and 10^9 at fixed y. The wall-model-relevant interval used in the text is $y/h \geq 0.15$. (*c*) Variations of β, $\langle B_{\rm eff}\rangle_y$ and $\langle C_{\rm eff}\rangle_y$ with Ra at $Ri_b = 1$, where $\langle\cdot\rangle_y$ denotes the arithmetic average over all sampled wall-normal locations in $0 \leq y/h \leq 1$.

Here, the overbar denotes an average over the four Rayleigh numbers at each fixed wall-normal position. This normalisation allows the variations of the two effective parameters to be compared despite their different absolute magnitudes. For the DNS-referenced WMLES cases at $Ri_b = 1$ and $Ra = 10^8$ and 10^9, the wall-model sampling height is $y_p/h = 0.15$ (table 2). We therefore use $y/h \geq 0.15$ as the wall-model-relevant interval when quoting the variations of the effective parameters. Over this interval, the maximum relative deviation of $B_{\rm eff}$ is approximately 25%, whereas that of $C_{\rm eff}$ remains below 5%. Figure 26(*c*) further shows the dependence on Ra of β and representative values of the two effective parameters. For each case, $\langle B_{\rm eff}\rangle_y$ and $\langle C_{\rm eff}\rangle_y$ denote arithmetic averages over all sampled wall-normal locations. As Ra increases, β becomes less negative, whereas $\langle B_{\rm eff}\rangle_y$ becomes more negative. Since β is independent of y within each case and $C_{\rm eff} = \beta B_{\rm eff}/2$, these opposing variations partially offset each other, resulting in a substantially weaker variation of $\langle C_{\rm eff}\rangle_y$ over the available DNS range.

References

del Álamo, J. C., Jiménez, J., Zandonade, P. & Moser, R. D. 2004 Scaling of the energy spectra of turbulent channels. *J. Fluid Mech.* **500**, 135–144.

Aliabadi, A. A., Krayenhoff, E. S., Nazarian, N., Chew, L. W., Armstrong, P. R., Afshari, A. & Norford, L. K. 2017 Effects of roof-edge roughness on air temperature and pollutant concentration in urban canyons. *Boundary-Layer Meteorol.* **164** (2), 249–279.

Bae, H. J., Lozano-Durán, A., Bose, S. T. & Moin, P. 2019 Dynamic slip wall model for large-eddy simulation. *J. Fluid Mech.* **859**, 400–432.

Balaji, C., Hölling, M. & Herwig, H. 2008 A temperature wall function for turbulent mixed convection from vertical, parallel plate channels. *Int. J. Therm. Sci.* **47** (6), 723–729.

Bernardini, M., Pirozzoli, S. & Orlandi, P. 2014 Velocity statistics in turbulent channel flow up to Re_τ = 4000. *J. Fluid Mech.* **742**, 171–191.

Boppana, V. B. L., Xie, Z.-T. & Castro, I. P. 2014 Thermal stratification effects on flow over a generic urban canopy. *Boundary-Layer Meteorol.* **153** (1), 141–162.

Bose, S. T. & Park, G. I. 2018 Wall-modeled large-eddy simulation for complex turbulent flows. *Annu. Rev. Fluid Mech.* **50**, 535–561.

Businger, J. A., Wyngaard, J. C., Izumi, Y. & Bradley, E. F. 1971 Flux-profile relationships in the atmospheric surface layer. *J. Atmos. Sci.* **28**, 181–189.

Castillo-Castellanos, A., Sergent, A., Podvin, B. & Rossi, M. 2019 Cessation and reversals of large-scale structures in square Rayleigh–Bénard cells. *J. Fluid Mech.* **877**, 922–954.

Chen, X., Gan, J. & Fu, L. 2025 Mean temperature–velocity relation and a new temperature wall model for compressible laminar and turbulent flows. *J. Fluid Mech.* **1009**, A39.

Chung, D. & McKeon, B. J. 2010 Large-eddy simulation of large-scale structures in long channel flow. *J. Fluid Mech.* **661**, 341–364.

Cossu, C. 2022 Onset of large-scale convection in wall-bounded turbulent shear flows. *J. Fluid Mech.* **945**, A33.

Cotton, M. A., Ismael, J. O. & Kirwin, P. J. 2001 Computations of post-trip reactor core thermal hydraulics using a strain parameter turbulence model. *Nucl. Eng. Des.* **208** (1), 51–66.

Dabbagh, F., Trias, F. X., Gorobets, A. & Oliva, A. 2017 A priori study of subgrid-scale features in turbulent Rayleigh-Bénard convection. *Phys. Fluids* **29** (10), 105103.

D'Alessandro, G., Marchioli, C. & Piomelli, U. 2025 Large-eddy simulation of the flow over a realistic riverine geometry. *J. Fluid Mech.* **1010**, A35.

Defraeye, T., Blocken, B. & Carmeliet, J. 2012 CFD simulation of heat transfer at surfaces of bluff bodies in turbulent boundary layers: evaluation of a forced-convective temperature wall function for mixed convection. *J. Wind Eng. Ind. Aerodyn.* **104–106**, 439–446.

Dyer, A. J. 1974 A review of flux-profile relationships. *Boundary-Layer Meteorol.* **7**, 363–372.

Foken, T. 2006 50 years of the Monin–Obukhov similarity theory. *Boundary-Layer Meteorol.* **119**, 431–447.

Grötzbach, G. 1983 Spatial resolution requirements for direct numerical simulation of the Rayleigh–Bénard convection. *J. Comput. Phys.* **49** (2), 241–264.

Howland, C. J., Yerragolam, G. S., Verzicco, R. & Lohse, D. 2024 Turbulent mixed convection in vertical and horizontal channels. *J. Fluid Mech.* **998**, A48.

Hu, X., Yang, X. & Park, G. I. 2024 On the grid convergence of wall-modeled large-eddy simulation. *J. Comput. Phys.* **504**, 112884.

Jayaraman, B. & Brasseur, J. G. 2021 Transition in atmospheric boundary layer turbulence structure from neutral to convective, and large-scale rolls. *J. Fluid Mech.* **913**, A42.

Jayatilleke, C. L. V. 1969 The influence of Prandtl number and surface roughness on the resistance of the laminar sublayer to momentum and heat transfer. *Prog. Heat Mass Transfer* **1**, 193–321.

Kawai, S. & Larsson, J. 2012 Wall-modeling in large eddy simulation: Length scales, grid resolution, and accuracy. *Phys. Fluids* **24** (1), 015105.

Kenjereš, S. & Hanjalić, K. 2006 LES, T-RANS and hybrid simulations of thermal convection at high Ra numbers. *Int. J. Heat Fluid Flow* **27** (5), 800–810.

Kim, K. C. & Adrian, R. J. 1999 Very large-scale motion in the outer layer. *Phys. Fluids* **11** (2), 417–422.

Kuwata, Y. & Suga, K. 2021 Wall-modeled large eddy simulation of turbulent heat transfer by the lattice Boltzmann method. *J. Comput. Phys.* **433**, 110186.

Lau, G. E., Yeoh, G. H., Timchenko, V. & Reizes, J. A. 2013 Large-eddy simulation of turbulent buoyancy-driven flow in a rectangular cavity. *Int. J. Heat Fluid Flow* **39**, 28–41.

Lee, M. & Moser, R. D. 2015 Direct numerical simulation of turbulent channel flow up to $Re_\tau \approx 5200$. *J. Fluid Mech.* **774**, 395–415.

Liu, H.-C., Xu, C.-X. & Huang, W.-X. 2025 A total-shear-stress-conserved wall model for large-eddy simulation of high-Reynolds number wall turbulence. *J. Comput. Phys.* **534**, 114029.

Liu, X., Pullin, D. I., Cheng, W. & Luo, X. 2026 Wall-modelled large-eddy simulations of the neutral atmospheric boundary layer over rough homogeneous and heterogeneous surfaces. *J. Fluid Mech.* **1037**, A1.

Madhusudanan, A., Illingworth, S. J., Marusic, I. & Chung, D. 2022 Navier-Stokes–based linear model for unstably stratified turbulent channel flows. *Phys. Rev. Fluids* **7** (4), 044601.

Maulik, R. & San, O. 2017 A dynamic subgrid-scale modeling framework for Boussinesq turbulence. *Int. J. Heat Mass Transf.* **108**, 1656–1675.

Monkewitz, P. A. & Nagib, H. M. 2023 The hunt for the Kármán 'constant' revisited. *J. Fluid Mech.* **967**, A15.

Nicoud, F. & Ducros, F. 1999 Subgrid-scale stress modelling based on the square of the velocity gradient tensor. *Flow Turbul. Combust.* **62**, 183–200.

Paulson, C. A. 1970 The mathematical representation of wind speed and temperature profiles in the unstable atmospheric surface layer. *J. Appl. Meteorol.* **9**, 857–861.

Piomelli, U. & Balaras, E. 2002 Wall-layer models for large-eddy simulations. *Annu. Rev. Fluid Mech.* **34** (1), 349–374.

Pirozzoli, S., Bernardini, M. & Orlandi, P. 2016 Passive scalars in turbulent channel flow at high Reynolds number. *J. Fluid Mech.* **788**, 614–639.

PIROZZOLI, S., BERNARDINI, M., VERZICCO, R. & ORLANDI, P. 2017 Mixed convection in turbulent channels with unstable stratification. *J. Fluid Mech.* **821**, 482–516.

PIROZZOLI, S. & ORLANDI, P. 2021 Natural grid stretching for DNS of wall-bounded flows. *J. Comput. Phys.* **439**, 110408.

SALESKY, S. T. & ANDERSON, W. 2018 Buoyancy effects on large-scale motions in convective atmospheric boundary layers: implications for modulation of near-wall processes. *J. Fluid Mech.* **856**, 135–168.

SCAGLIARINI, A., EINARSSON, H., GYLFASON, Á. & TOSCHI, F. 2015 Law of the wall in an unstably stratified turbulent channel flow. *J. Fluid Mech.* **781**, R5.

SOUCASSE, L., PODVIN, B., RIVIÈRE, P. & SOUFIANI, A. 2019 Proper orthogonal decomposition analysis and modelling of large-scale flow reorientations in a cubic Rayleigh–Bénard cell. *J. Fluid Mech.* **881**, 23–50.

SUN, J. E. K. I. & FU, L. 2026 A new mean temperature model for incompressible wall-bounded turbulence over a wide range of Prandtl numbers. *J. Fluid Mech.* **1035**, A34.

WANG, A., YANG, X. I. A. & OVCHINNIKOV, M. 2024 An investigation of LES wall modeling for Rayleigh–Bénard convection via interpretable and physics-aware feedforward neural networks with DNS. *J. Atmos. Sci.* **81** (2), 435–458.

XU, A., LI, R.-Q. & XI, H.-D. 2025 Temporal modulation on mixed convection in turbulent channels. *J. Fluid Mech.* **1006**, A11.

YERRAGOLAM, G. S., HOWLAND, C. J., STEVENS, R. J. A. M., VERZICCO, R., SHISHKINA, O. & LOHSE, D. 2024 Scaling relations for heat and momentum transport in sheared Rayleigh–Bénard convection. *J. Fluid Mech.* **1000**, A74.

YILMAZ, I. 2021 A novel buoyancy-modified subgrid-scale model for large-eddy simulation of turbulent convection. *Int. J. Numer. Method H.* **31** (8), 2509–2533.

ZHANG, F., YANG, X. & HE, G. 2026 A differentiable wall-modeled large-eddy simulation method for high-Reynolds-number wall-bounded turbulent flows. *J. Comput. Phys.* **557**, 114835.

ZHANG, F., ZHOU, Z., YANG, X. & HE, G. 2025 Knowledge-integrated additive learning for consistent near-wall modelling of turbulent flows. *J. Fluid Mech.* **1011**, R1.